universität wien

MASTERARBEIT

Titel der Masterarbeit

A neutral particle detector for photodetachment studies

Verfasser

Johannes Lahner, BSc

angestrebter akademischer Grad

Master of Science (MSc)

Wien, 2014

Studienkennzahl lt. Studienblatt:	A 066 876
Studienrichtung lt. Studienblatt:	Masterstudium Physik
Betreuer:	Univ.-Prof. Dipl.-Ing. Dr. Robin Golser

Meinen Eltern

Abstract

The aim of this thesis was to design and to construct a neutral particle detector for ILIAS (Ion Laser InterAction Setup) and to perform a test measurement using an appropriate detection setup. ILIAS was developed at the University of Vienna at the Faculty of Physics, Isotope Research and Nuclear Physics, to explore selective optical filtering of negatively charged ions via laser photodetachment. A negative ion beam spectrometer provides mass separated negatively charged ions comparable to the low energy side of an AMS facility. This particle beam is overlapped collinearly with a laser beam, hence, negative ions with electron affinities below the laser energy can be neutralized and subsequently filtered using an electrostatic beam bender. In this way ILIAS combined with an AMS facility opens up a new promising method for isobar suppression.

The neutral particle detector is required in order to measure the efficiency of selective suppression with ILIAS. For this purpose the ion beam is overlapped with a laser beam for a second time after the electrostatic beam bender to determine the fraction of the remained unwanted isobars. As the produced neutrals cannot be deflected by electric or magnetic fields the detector has to be positioned in the axis of the laser beam and, thus, be transparent for the used laser light. Hence, the detector is composed of a conductively-coated glass plate. When particles impinge on the glass plate secondary electrons are ejected. The emitted electrons are detected using a suitable ion optical system and a channel electron multiplier.

Furthermore, an appropriate setup was installed in order to test the new detector. The setup was designed in such a way that it can be additionally used for the measurement of the efficiency of selective isobar suppression with ILIAS. The correct operation of the detector was tested by neutralizing $^{12}C^-$ and $^{12}CH^-$ ions, respectively, via laser photodetachment. The results show that the detection setup and the developed neutral particle detector work and fulfill the wanted requirements. The time resolution of the detector is <10 ns FWHM and the maximum count rate is $5{\cdot}10^6$ cps. The background signal depends mainly on the vacuum conditions since ions are also neutralized due to collisional detachment. The background signal by $^{12}CH^-$ is significantly higher than by $^{12}C^-$.

Zusammenfassung

Ziel dieser Masterarbeit war es, einen Neutralteilchendetektor für ILIAS (Ion Laser Inter-Action Setup) zu entwickeln, aufzubauen und mit einem geeigneten Messaufbau zu testen. ILIAS wurde an der Universität Wien an der Fakultät für Physik, Isotopenforschung und Kernphysik, entwickelt, um die selektive optische Filterung negativ geladener Ionen durch Laser-Photodetachment zu untersuchen. Mithilfe eines Massenspektrometers, vergleichbar mit der Niederenergieseite einer AMS Anlage, können massenseparierte Ionenstrahlen erzeugt werden. Wird dieser Teilchenstrahl mit einem Laser kollinear überlagert, so können jene negativen Ionen, deren Elektronenaffinität geringer ist als die Laserenergie, neutralisiert und anschließend mit einem elektrostatischen Ablenker gefiltert werden. Auf diese Weise eröffnet ILIAS in Kombination mit einer AMS Anlage eine vielversprechende neue Methode zur Isobarenunterdrückung.

Der Neutralteilchendetektor wird benötigt, um die Effizienz der selektiven Isobarenunterdrückung von ILIAS zu messen. Dazu wird der Ionenstrahl nach dem elektrostatischen Ablenker ein zweites Mal kollinear mit einem Laserstrahl überlagert um den Anteil der noch im Ionenstrahl befindlichen unerwünschten Isobare zu bestimmen. Da die so erzeugten Neutralteilchen nicht mehr abgelenkt werden können, muss sich der Detektor im Laserstahl befinden und somit für den verwendeten Laser transparent sein. Der Detektor wurde daher aus einem Glasplättchen mit einer leitenden Beschichtung aufgebaut. Die auftreffenden Neutralteilchen schlagen Sekundärelektronen aus der dünnen Beschichtung welche dann mittels geeigneter Ionenoptik zu einem Elektronenvervielfacher gelenkt und nachgewiesen werden.

Des Weiteren wurde ein geeigneter Messaufbau installiert um den neuen Detektor zu testen. Der Messaufbau wurde dabei so realisiert, dass er sich auch für die Messung der Effizienz der selektiven Isobarenuterdrückung von ILIAS eignet. Um die Funktionsfähigkeit des Detektors zu überprüfen, wurden $^{12}C^-$- beziehungsweise $^{12}CH^-$-Ionen durch Laser-Photodetachment neutralisiert. Die Ergebnisse dieser Messungen zeigen, dass der Messaufau und der Neutralteilchendetektor funktionieren und die erwarteten Anforderungen erfüllen. Der Detektor hat eine Zeitauflösung von <10 ns FWHM und eine maximale Zählrate von $5 \cdot 10^6$ cps. Das Hintergrundsignal ist aufgrund der Neutralisation von Ionen durch Kollisionen mit Restgas in erster Linie vom Vakuum abhängig und für $^{12}CH^-$ deutlich höher als für $^{12}C^-$.

Contents

1 Introduction 1

1.1 Motivation . . . 1

1.2 Outline . . . 1

2 ILIAS – Ion Laser InterAction Setup 3

2.1 Principles and Motivation . . . 3

2.2 Cases to be studied in the course of the ILIAS project . . . 8

2.2.1 ^{14}C . . . 8

2.2.2 ^{60}Fe . . . 8

2.2.3 ^{182}Hf . . . 8

2.3 Methods and Setup . . . 9

2.3.1 Negative ion beam spectrometer . . . 9

2.3.2 The gas-filled radio frequency ion beam cooler . . . 11

2.4 Measurement of the efficiency of selective suppression . . . 11

3 The Neutral Particle Detector 15

3.1 Principles . . . 15

3.2 Components . . . 15

3.2.1 The glass plate . . . 15

3.2.2 Ion optics . . . 16

3.2.3 Channel electron multiplier (CEM) . . . 16

3.3 Construction and design . . . 17

3.3.1 Simulation with SIMION 8.0 . . . 17

3.3.2 Setup and production . . . 19

3.3.3 Electrical connections . . . 22

4 Detection setup 25

4.1 Negative ion beam spectrometer . . . 26

4.2 Magnetic quadrupole doublet . . . 26

4.3 Beam benders . . . 26

4.4 Device for precise overlap of ion- and laser beam . . . 30

4.5 Laser . . . 31

4.6 Signal processing (neutral particle detector) . . . 32

4.7 Aperture to reduce background signal . . . 33

4.8 Estimation of the count rate of photodetached ions . . . 37

5 Measurements and results **39**
5.1 $^{12}C^-$ 39
5.2 $^{12}CH^-$ 42
5.3 $^{12}C^-$ versus $^{12}CH^-$ 43
5.4 Discussion and outlook 43

Appendices **45**

A Engineering drawing of the used CEM **47**

B Characteristics of standard CEMs **49**

C Geometry file for SIMION **51**

D Engineering drawing of the quadrupole beam bender by DREEBIT **53**

E Characteristics of the preamplifier WMT PAD01A **55**

Bibliography **57**

Acknowledgments **61**

Curriculum vitae **63**

List of Figures

2.1 Principle of selective optical filtering. 5
2.2 Illustration of the laser photodetachment fraction for Co^- ions. 6
2.3 Schematic view of the gas-filled rf quadrupole ion cooler. 7
2.4 Measured ion currents after the RFQ when the laser is on/off. 7
2.5 Schematic illustration of the setup of ILIAS. 10
2.6 Experimental setup to measure the efficiency of selective suppression. 12
2.7 Schematic of a surface barrier Si detector. 12
2.8 Detection principle of a metallic magnetic calorimeter. 13

3.1 Schematic representation of the neutral particle detector. 15
3.2 Image and cut view of standard channel electron multipliers. 16
3.3 Characteristics of standard CEMs. 17
3.4 Histogram of time of flight of secondary electrons. 19
3.5 Final design of the detector illustrated in SIMION 8.0. 20
3.6 Engineering drawings for the holders. 21
3.7 Holder for glass plate and ion optical system. 21
3.8 Coated glass plate and ion optical system mounted on a linear drive. 22
3.9 Channel electron multiplier mounted on a blank flange. 23
3.10 Neutral particle detector installed in six-way cross piece. 23
3.11 Wiring of the CEM. 24

4.1 Schematic view of ILIAS and the detection setup. 25
4.2 Electrostatic quadrupole beam bender by *DREEBIT*. 27
4.3 Simulation of the beam geometry in the quadrupole beam bender. 28
4.4 In-house developed and manufactured beam bender. 29
4.5 Simulation of the beam geometry in the in-house developed beam bender. 29
4.6 Device for precise overlap of ion- and laser beam. 30
4.7 Influence of the temperature of the laser system on the light spectra. 31
4.8 Setup of the laser. 32
4.9 Signal processing (neutral particle detector). 32
4.10 Representative image of the used preamplifier/discriminator for the CEM. 33
4.11 Aperture to reduce background signal caused by electrons. 35

5.1 Photodetachment results for $^{12}C^-$. 41
5.2 Photodetachment results for $^{12}CH^-$. 42

A.1 Engineering drawing of the used CEM. 48

B.1 Characteristics of standard CEMs. 49

D.1 Engineering drawing of the DREEBIT quadrupole beam bender. 53

List of Tables

3.1 Characteristics of standard CEMs. 17

4.1 Power dissipation of the laser beam due to entrance/exit window. 32
4.2 Count rate of the CEM for different cases. 35
4.3 Background signal as a function of the vacuum. 36
4.4 Count rate of the detector as a function of the applied voltage to the focus ring. 36

5.1 Comparison of the results of $^{12}C^-$ and $^{12}CH^-$. 43

E.1 Characteristics of the used preamplifier WMT PAD01A. 55

1 Introduction

1.1 Motivation

This thesis was conducted at ILIAS (Ion Laser InterAction Setup) at the University of Vienna. The facility was developed for investigating selective optical filtering of negatively charged ions via laser photodetachment. The setup provides mass separated negatively charged ion beams with energies of 10 – 30 keV comparable to the low energy side of an AMS (Accelerator Mass Spectrometry) facility. However, the ion beam is overlapped collinearly with a laser beam in order to neutralize anions with electron affinities below the laser energy. This shall be used as an element-selective filtering technique for negative ion beams. The main requirement for effective filtering is that the electron affinity of the unwanted ions is lower than the electron affinity of the species of interest. Furthermore, the interaction time of the ion- and the laser beam has to be long enough to neutralize practically 100 % of the ions to be filtered.

This can be accomplished using a gas-filled radio frequency quadrupole ion cooler. It decelerates the ion beam from the keV range to some 10 eV by an appropriate ion optical system. Due to collisions of the ions with the buffer gas inside the quadrupole the ions are cooled to thermal energies. In this way the interaction time of the ions and the laser beam is extended from microseconds to some milliseconds. At the exit of the rf quadrupole cooler the remaining ions are extracted and re-accelerated to their original energy [1].

ILIAS combined with an AMS facility like VERA (Vienna Environmental Research Accelerator) [2] provides the possibility to suppress interfering isobars by ion-photon interaction and, thus, is a promising technique to improve the sensitivity of AMS for rare isotopes. Hence, several radio isotopes, where intense isobaric interference currently hinders detection by AMS, could become accessible at their natural levels.

1.2 Outline

The main objectives of this thesis were to

1 **Design and construct a neutral particle detector, to**

2 **Build an appropriate detection setup, and to**

3 **Neutralize atomic and molecular anions, respectively, via laser photodetachment to test the new detector.**

The steps to achieve these objectives were:

- Definition of the requirements and specifications of the neutral particle detector
- Performance of computer simulations for efficient setup of the detector
- Manufacturing and installation of the detector and the components of the detection setup
- Implementation of the signal processing
- Investigation of the neutralization of $^{12}C^-$ and $^{12}CH^-$ via laser photodetachment

In the following chapter the principles and the motivation of ILIAS and an abridged compilation of possible applications will be presented. Furthermore, the setup and the operating mode will be described in detail. Different possibilities of (neutral) particle detection and the requirement of a neutral particle detector at ILIAS will be specified in section 2.4.

The functional principle of the neutral particle detector and a detailed characterization of its components will be given in chapter 3. Also, the performance of computer simulations for an efficient setup of the detector and the resulting design and construction, respectively, will be explained.

In order to test the performance of the new detector an appropriate detection setup was built. Various components such as electrostatic beam benders, a device for precise overlap of the laser and the ion beam, Faraday cups, an aperture to reduce the background signal, and a laser had to be installed. Besides, devices for the implementation of the signal processing were integrated. Details can be found in chapter 4.

In chapter 5 the results of the neutralization of $^{12}C^-$ and $^{12}CH^-$ ions via laser photodetachment will be presented. On the basis of these results conclusions concerning the functionality of the detector and the detection setup will be drawn and estimated count rates will be compared to the measured count rates. Moreover, suggestions for improvement of the background signal and, thus, the sensitivity of the measurement setup will be discussed.

2 | ILIAS – Ion Laser InterAction Setup

2.1 Principles and Motivation

Radio nuclides are of great interest to various fields in science and technology such as medicine, industry, astronomy, climate research, and many more [3]. There are basically two methods for their detection: Decay counting and mass spectrometry. Both methods have to deal with the same problems in the detection of radio nuclides as they have typically low abundances between 10^{-12} and 10^{-18} g/g [4]. Additionally, the interference of other species in the measurement is possible.

1. Decay counting
   Decay counting measures the number of decays that occur in a defined time interval. Subsequently, using the decay rate, one can determine the abundance of the radio nuclide of interest. This method is suitable for short-lived radio nuclides up to a half-life of approximately 10^3 years [4]. Above that, the required sample sizes and counting times are difficult to handle.

2. Mass spectrometry
   A conventional mass spectrometer analyzes substances by ionizing the material, focusing the produced ions into a beam and separating them according to their mass-to-charge ratio [5]. The beam energy is usually in the low keV range. Such a system can principally resolve even isobaric and molecular interferences but the efficiency is very low and, thus, the count rates of the wanted radio nuclides would still be comparable to decay counting. The detected currents of the corresponding stable isotopes would be in the nA range. Typical currents in an AMS system are in the order of some µA [6], however, the high efficiency is accomplished at the cost of the mass resolution, hence, a different approach to suppress interfering isobars has to be found.

Basically, it is feasible to suppress interfering isobars by chemistry. At first sight this method seems to be more effective than isobar suppression by physics due to the fact that the relevant physical properties of the particles for mass spectrometry are quite similar while the chemical properties are usually completely different. This statement is basically correct but applies only up to approximately six orders of magnitude. As soon as any stable interfering isobar is reduced to about 10^{-6} g/g no further improvement is achieved, since the chemical processing re-introduces as much of this nuclide as it removes. Levels of 10^{-12} and less are therefore absolutely inaccessible. [4]

Accelerator mass spectrometry (AMS) works basically like conventional mass spectrometry but at much higher energies (MeV range) and with a negative ion source which entails several significant advantages concerning isobar suppression [7].

- Negative ion source
  A cesium sputter source produces negative ions from a sample material. There are no stable atomic isobaric interferences in the case of ^{14}C, ^{26}Al, and ^{129}I, since ^{14}N, ^{26}Mg, and ^{129}Xe do not form stable negative ion [6]. Hence, one has only to deal with the molecular isobaric background.

- Stripping process
  The centerpiece of an AMS system is the tandem accelerator. Typical operating voltages are between 0.5 and 10 MV [8]. The negative ions are accelerated towards a positively charged terminal where they pass through a stripper gas or a thin carbon foil. By this process molecules break up and can be effectively removed with a mass spectrometer during the further procedure. After the stripping process the multiple positively charged ions are repelled from the positive terminal and accelerated to ground potential. By this means the high particle energies in the order of MeV are achieved.

- Energy loss of particles in matter
  Due to the high particle energies in AMS an additional method for isobar separation becomes available based on the different energy loss of particles in matter. This method will be explained using the example of ^{36}Cl. The interfering isobar is ^{36}S is stable and forms negative ions as readily as ^{36}Cl. In addition, the count rate of ^{36}S is typically three orders of magnitude higher than the ^{36}Cl rate. Despite that high isobaric background the two species can be effectively separated by using an ionization chamber [6]. Until a few years ago particle energies of $\sim$50 MeV were necessary to separate the two species. However, advanced ionization chambers have opened new possibilities for the separation of ^{36}Cl and ^{36}S below the Bragg peak at energies of 24 MeV, which are accessible with medium-sized accelerators [9, 10]. Thus ^{36}Cl has become a routine AMS-isotope at VERA.

  For a given particle energy this method of isobar discrimination is currently limited by a certain ratio of ΔZ/Z. The heaviest radio nuclide which is measured routinely at some laboratories is ^{60}Fe. The corresponding interfering isobar is ^{60}Ni i.e. ΔZ/Z=1/14 [4]. Explorative effort enabled even the separation of ^{93}Zr and ^{93}Nb (ΔZ/Z=1/40) [11] but for heavier radio nuclides a different approach has to be found.

A further possibility of isobar reduction is by photon–ion interaction. This method was applied by D. Berkovits et al. for the case of S/Cl and Co/Ni. It was found that typical cross sections for laser photodetachment are in the order of 10^{-17} cm^2 [12, 13]. The principle of this process is to neutralize the interfering isobar by laser photodetachment. This method called selective optical filtering presupposes that the electron affinity of the interfering isobar is lower than that of the isotope of interest. If this applies, a laser with suitable photon energy can be chosen to neutralize the unwanted isobar only (Fig. 2.1). The photodetachment cross section around the threshold energy is described by the Wigner-law:

$$\sigma \propto (E - E_{EA})^{l+1/2}$$

where E is the laser energy, E_{EA} the electron affinity of the unwanted isobar, and l is the azimuthal quantum number of the electron [14]. As this is an non-resonant process the energy of the laser has to be just sufficiently higher than the electron affinity of the interfering isobar. The probability of photodetachment, f, is a function of the incident photon flux Φ, the photodetachment cross section σ and the laser-ion interaction time t.

$$f = 1 - e^{-\sigma\Phi t} \tag{2.1}$$

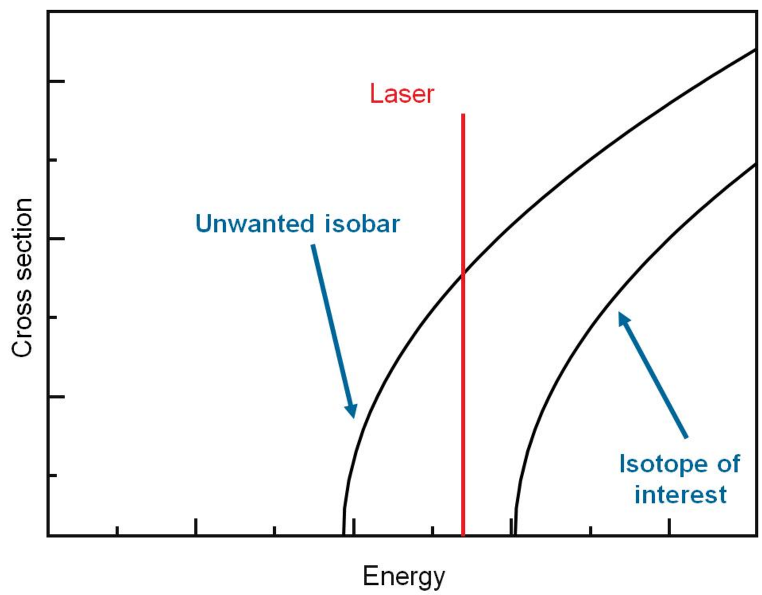

Figure 2.1: Qualitative illustration of the photodetachment cross section of the interfering isobar and the isotope of interest as a function of the energy. The cross section around threshold is described by the Wigner-law: $\sigma \propto (E - E_{EA})^{l+1/2}$, where E is the laser energy, E_{EA} the electron affinity of the unwanted isobar, and l is the azimuthal quantum number of the electron. In this illustration l is assumed to be zero. Selective optical filtering presupposes that the electron affinity of the interfering isobar is lower than that of the isotope of interest. A laser with an appropriate energy neutralizes the unwanted isobar while the isotope remains unchanged. Figure taken from [14].

D. Berkovits et al. used in their experiments ions with energies of ~100 keV which were interacting with the laser beam over a distance of 1.2 m. Due to the short interaction time of a few microseconds the degree of isobar suppression was too small for practical use since virtually all interfering isobars have to be neutralized and removed in the optical filtering process. Therefore, given the available laser power the interaction distance has to be several 100 times longer to achieve the required interaction time in the range of milliseconds between the ions and the photons. Figure 2.2 shows the calculated laser photodetachment fraction for Co^- ions as a function of interaction time of laser and ion beam at different laser powers.

As it is practically impossible to overlap the ion beam and the laser beam over some hundreds of meters Liu et al. [15] and Andersson et al. [16] used a linear gas-filled radio frequency quadrupole ion cooler (RFQ) to decelerate the ions from the keV range to some 10 eV by an appropriate ion optical system. Due to collisions of the ions with the buffer gas inside the RFQ the ions are cooled to thermal energies (Fig. 2.3). Thus, the interaction time was extended to the required range of milliseconds and thereby the efficiency of

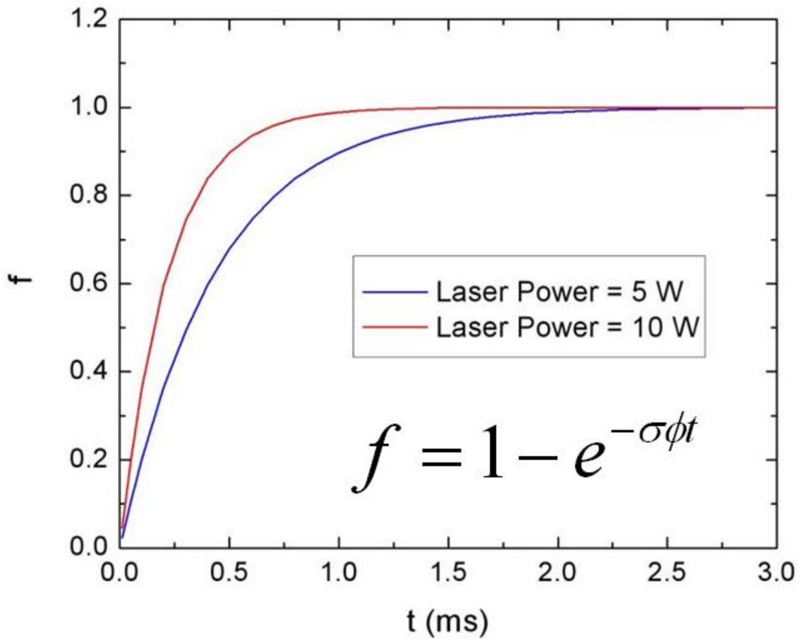

Figure 2.2: This figure illustrates the calculated laser photodetachment fraction f for Co^- ions as a function of the interaction time of the laser and the ion beam at different laser powers. The wavelength of the used laser is $\lambda = 1064\,\mathrm{nm}$ ($\hat{=}\,1.166\,\mathrm{eV}$), the laser beam size and the ion beam size is $\mathrm{d} = 3\,\mathrm{mm}$, and the photodetachment cross section is $\sigma(\mathrm{Co}^-) = 6 \cdot 10^{-18}\,\mathrm{cm}^2$. The fraction f of negative ions removed by photodetachment is a function of the incident photon flux Φ, the photodetachment cross section σ and the laser-ion interaction time t. Figure taken from [14].

photodetachment increased to almost 100 %. Consequently the new technique provided nearly 100 % suppression of interfering stable isobars in negative ion beams. For a given photodetachment cross section and ion residence time in the RFQ the detachment efficiency is limited by the laser power (see equation 2.1). Using a commercially available laser with 1064 nm ($\hat{=}\,1.166\,\mathrm{eV}$) and ∼6 W the photodetachment efficiency for $^{59}\mathrm{Co}^-$ ions (EA = 0.663 eV [17]) is 99.99 % and for $^{58}\mathrm{Ni}^-$ ions (EA = 1.157 eV [17]) ∼20 % [16] (Fig. 2.4).

In the view of these results laser photodetachment combined with a gas-filled radio frequency quadrupole ion cooler is a promising technique for isobar suppression at AMS facilities especially for heavy radio nuclides. An alternative approach for isobar suppression is by anion-gas reactions in an RFQ gas cell. A detailed description of this (chemical) method can be found elsewhere [18, 19].

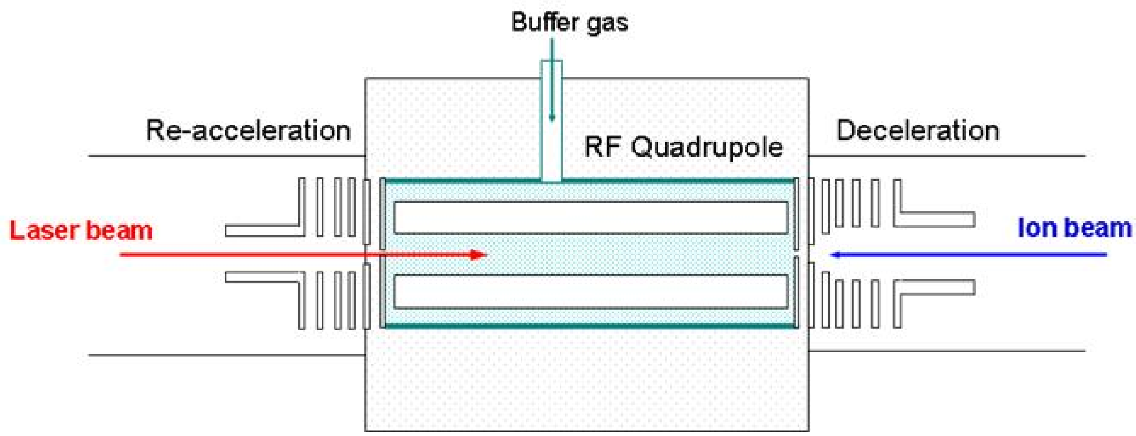

Figure 2.3: Schematic view of the gas-filled radio frequency quadrupole ion cooler (RFQ). The ions are decelerated from the keV range to some 10 eV by an appropriate ion optical system. Due to collisions of the ions with the buffer gas inside the RFQ the ions are cooled to thermal energies to extend the interaction time between the laser beam and the ion beam. Thus the detachment rate is significantly increased. Figure taken from [15].

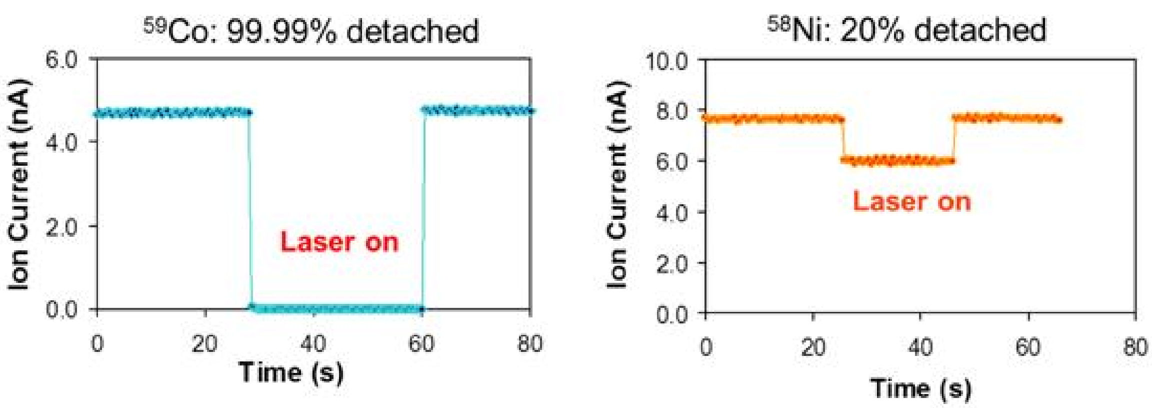

Figure 2.4: Measured ion currents after the RFQ when the laser beam is turned on/off. When the laser is on 99.99 % of $^{59}Co^-$ (EA = 0.663 eV [17]) and 20 % of $^{58}Ni^-$ (EA = 1.157 eV [17]) ions are neutralized using a commercially available laser with 1064 nm (≙ 1.166 eV) and ∼6 W [16]. This demonstration experiment was performed at Oak Ridge National Laboratory. Figure taken from [14].

2.2 Cases to be studied in the course of the ILIAS project

2.2.1 ^{14}C

C-isotopes are of special interest in nuclear science because of the radio carbon dating method. In order to obtain sufficiently precise results for the ^{14}C content it is crucial to suppress the interfering molecular isobars $^{13}CH^-$ and $^{12}CH_2^-$. The electron affinity of C^- ((1.262119 ± 0.000020) eV) is higher than that of the molecular anions CH^- ((1.238 ± 0.008) eV) and CH_2^- ((0.652 ± 0.006) eV) [17]. Hence, using a laser with an appropriate wavelength (983 nm ≅ 1.262 eV) enables the suppression of the unwanted CH molecules via laser photodetachment. This additional depletion of $^{13}CH^-$ and $^{12}CH_2^-$ can be beneficial especially for small AMS facilities. With more development work even ^{14}C dating using only optical filtering could be possible. [4]

2.2.2 ^{60}Fe

The radio isotope ^{60}Fe ($T_{1/2}$=(2.62 ± 0.04) Ma [20]) is of great interest for astronomy, since it is naturally produced only by stellar nucleosynthesis [21, 22] or in small amounts via spallation reactions with cosmic rays [23, 24]. The production via spallation is only relevant for extraterrestrial objects because of the atmospheric shielding of the earth from cosmic rays. Hence, ^{60}Fe traces measured on earth can indicate a supernova explosion in the vicinity of the earth during the past several millions of years but also other radio isotopes like ^{146}Sm, ^{182}Hf, and ^{244}Pu are possible candidates for supernova detection [25]. Since those nuclides are produced in much smaller quantities ^{60}Fe seems to be a unique indicator for supernova events.

AMS measurements of ^{60}Fe are interfered by the strong presence of the stable isobar ^{60}Ni (26 % natural isotopic abundance [26]). Currently the separation of ^{60}Ni depends on the different energy loss of particles in matter described in section 2.1. In the case of ^{60}Fe this technique requires high particle energies to reach the needed detection level of 10^{-15} for the isotope ratio ^{60}Fe/Fe [25]. The required high ion energies are only supplied at large AMS facilities with terminal voltages above 10 MV. Isobar suppression via laser photodetachment would enable the measurement of ^{60}Fe at AMS facilities like VERA with terminal voltages of about 3 MV and, thus, open up the possibility to verify results like [23, 25] at different laboratories. However, direct optical filtering is not possible since the electron affinity of the Fe^- ions ((0.151 ± 0.003) eV) is much lower than that of the Ni^- ions ((1.15716 ± 0.00012) eV) but the situation is reversed for the molecular ions FeH^- ((0.934 ± 0.011) eV) and NiH^- ((0.481 ± 0.007) eV) [17]. These hydride molecular anions can be produced in adequate amounts in a cesium sputter ion source [26].

2.2.3 ^{182}Hf

^{182}Hf is a long-lived radio isotope which decays to the stable isotope ^{182}W by beta radiation. Due to its half-life of (8.9 ± 0.09) Ma [27] and the fact that the isotope is naturally produced only in supernovae all ^{182}Hf present at the early stage of the solar system has decayed. Thus, any Hafnium radio isotope detected today is either of anthropogenic origin or stems from nearby supernovae [28]. The detection of the radio isotope ^{60}Fe in a deep-sea ferromanganese crust indicates a supernova explosion at a distance of a few 10 pc around 2.8 Ma ago [25].

These measurements spurred the search for a detection of a signature of ^{182}Hf to confirm the ^{60}Fe results. Based on these measurements the roughly estimated isotopic ratio of ^{182}Hf/^{180}Hf is in the range of 10^{-13} but since the assumptions of this estimation has been over simplified the value of the isotopic ratio can be even lower by orders of magnitude [28]. Hence, the only possible chance to detect the low concentrations of ^{182}Hf sedimented in deep sea after a supernova event is by AMS.

As mentioned before, ^{182}Hf decays to the stable isotope ^{182}W, which causes the main isobaric background signal in an AMS measurement and cannot be separated from ^{182}Hf at energies of 12–20 MeV available at medium sized accelerators like VERA [28, 29]. Thus, the suppression of the interfering isobar ^{182}W is necessary. Using HfF_4 as target material in the cesium sputter ion source and extracting HfF_5^- enables a reduction of ^{182}W by around four orders of magnitude since the production probability of the tungsten molecule is much lower than that of the hafnium molecule. This leads to a detection limit for the ^{182}Hf/^{180}Hf isotopic ratio in the range of 10^{-11} [29]. Hence, further suppression of ^{182}W by at least two orders of magnitude is necessary to confirm the supernova signal indicated by ^{60}Fe measurements referred in [25]. To achieve the required suppression by laser photodetachment the electron affinity of WF_5^- has to be lower than that of HfF_5^-. By now only few experimental data for the electron affinity of the molecules WF_5^- and HfF_5^- are known but measurements at GUNILLA indicated that the electron affinity of the tungsten molecule is indeed lower than that of the hafnium molecule [30]. Also, Leopold et al. showed that the photodetachment cross section for WF_5^- is at least 100 times larger than for HfF_5^- at a wavelength of 266 nm [31]. Hence, laser photodetachment together with AMS is a promising technique to reach the required ^{182}Hf/^{180}Hf isotopic ratio level of 10^{-13} and less.

2.3 Methods and Setup

ILIAS is set up at the University of Vienna since 2010 for photodetachment studies aiming at AMS applications. The setup consists basically of a negative ion beam spectrometer, a radio frequency quadrupole ion cooler, a laser, and different detectors such as Faraday cups and the neutral particle detector. The essential parts will be described in the following sections. As soon as the technique has been successfully developed parts of ILIAS will be coupled to the VERA AMS facility. The required structural measures are already in progress.

2.3.1 Negative ion beam spectrometer

In order to test the rf quadrupole ion cooler for different scientific relevant cases an appropriate ion beam spectrometer is required which provides mass separated negatively charged ion beams (Fig. 2.5). The main components will be described in detail in the following:

- Ion source
  ILIAS uses a single cathode cesium sputter ion source to produce the negative ions. Cesium is heated by an oven and vaporizes. Some of this Cs vapor condenses on the sample material (cathode) and some gets ionized by a heated tantalum surface (anode). Due to a potential difference between the cathode and the anode the Cs^+ ions are accelerated and focused towards the sample material. Thus, particles are sputtered from the cathode and some pick up electrons when they go through the condensed cesium

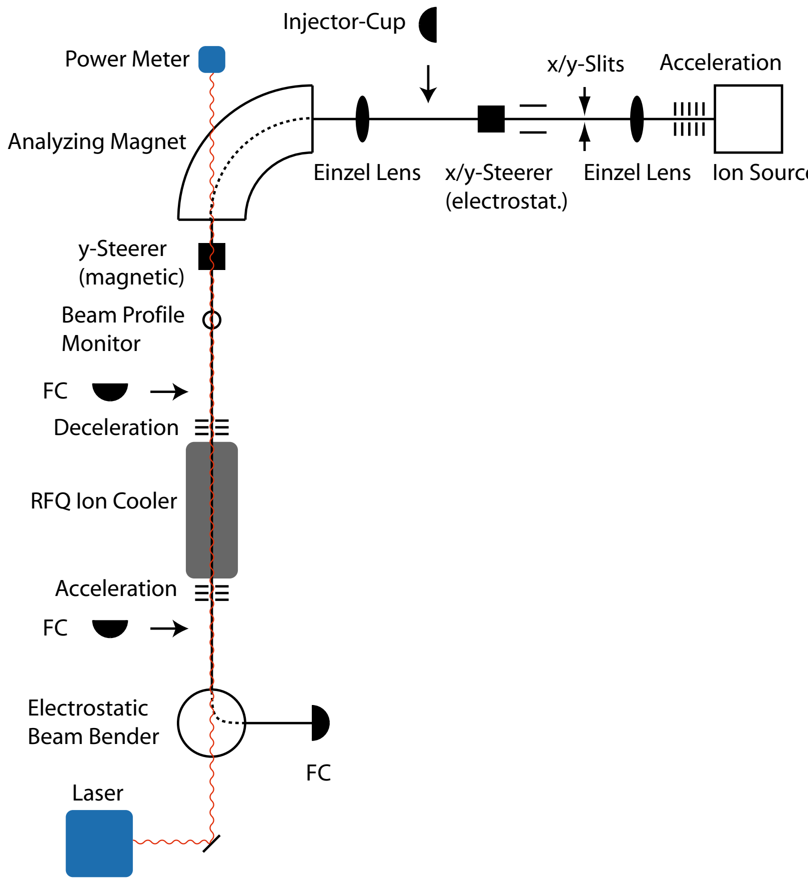

Figure 2.5: Schematic illustration of the setup of ILIAS. An ion beam spectrometer provides mass separated negatively charged ion beams which are overlapped collinearly with a laser beam in order to suppress interfering isobars by laser photodetachment. The RFQ ion cooler ensures that the interaction time between the ions and the photons is sufficiently long to neutralize practically all isobars.

coating. The negative ions produced in this process are extracted from the ion source by the applied high voltage. In this way the cesium sputter ion source can produce various atomic and molecular negative ions. [32] A particle energy in the range of $10 - 30\,\mathrm{keV}$ ensures efficient injection into the rf quadrupole ion cooler.

- Analyzing magnet
  Magnetic filters are selecting ions with a certain momentum to charge ratio p/q corresponding to the Lorentz force, i.e. the magnetic deflection increases linearly according to the velocity of the charged particles. Hence, for a given energy the analyzing magnet separates the ions for $\mathrm{m/q^2}$:

$$\underbrace{qvB}_{\text{Lorentz-force}} = \underbrace{\frac{mv^2}{\rho}}_{\text{Centripetal force}}$$

Rewriting this equation yields:

$$\underbrace{B\rho}_{\text{Magnetic rigidity}} = \frac{p}{q}$$

$$\left(B\rho = \frac{\sqrt{2mE}}{q}\right)$$

The analyzing magnet being used is a 90° double focusing magnet which is capable of bending negative ion beams of masses up to 300 amu, as the heaviest molecule relevant for this project will be $^{186}WF_5^-$ with a mass of 281 amu [4, 33].

2.3.2 The gas-filled radio frequency ion beam cooler

Gas-filled radio frequency ion beam coolers can be used for cooling, accumulating and bunching ion beams and, thus, find application in many fields in nuclear physics. Most ion beam coolers are designed for positive ions. Cooling negative ions is more delicate, since their electron affinities are only in the order of some eV and, thus, they can be neutralized by collisions with the buffer gas. To minimize these losses and to increase transmission the ion cooler has to be designed to efficiently remove the buffer gas in the injection stage of the device. In addition, the kinetic energy of the ions has to be decreased from the keV range to energies of some 10 eV by an appropriate ion optical system to avoid losses due to collisional detachment of the electron when the ions enter the cooler [1, 34]. In this way Liu et al. [1] showed that a negative ion transmission up to 50 % is reachable.

2.4 Measurement of the efficiency of selective suppression

In order to measure the photodetachment efficiency in a gas-filled radio frequency quadrupole ion cooler Liu et al. [15] used an electrostatic beam bender to deflect the ions extracted from the RFQ cooler to an off-axis Faraday cup. However, when 99.99 % suppression is achieved as described in [16] the sensitivity of the picoampere meter used with the Faraday cup is insufficient. Thus, in order to measure the efficiency of isobar suppression by laser photodetachment at ILIAS the setup (Fig. 2.5) is extended by a probe region where the particle beam will be overlapped collinearly with a laser beam for a second time (Fig. 2.6). This is accomplished using two electrostatic beam benders. Negative ions leaving the RFQ cooler are deflected by the first beam bender into a probe region where the ion beam is once more overlapped with a laser beam. Neutrals produced in the probe region move on in a straight direction to a neutral particle detector while the remaining ions are bent into a Faraday cup by the second beam bender. This method ensures that only the fraction of the remaining unwanted isobars in the ion beam after the RFQ cooler is detected by the neutral particle detector. A similar setup is described in [16].

Hence, the efficiency of the selective isobar suppression in the ion cooler is determined by the number of neutrals produced in the second photodetachment attempt. There are basically three possibilities to detect neutral particles. The choice of the method depends on the energy of the incident particles, the required time- and energy resolution, and the specific surrounding conditions of the measurement setup:

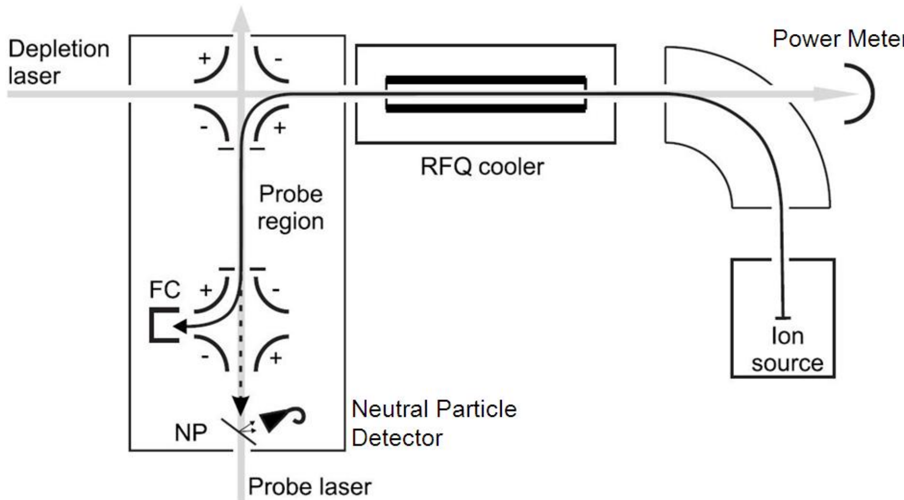

Figure 2.6: Schematic view of the experimental setup to measure the efficiency of selective suppression via laser photodetachment. Ions which transited the RFQ cooler are deflected by an electrostatic field into a probe region were the ion beam is once more overlapped with a laser beam. Neutrals produced in the probe region move on in a straight direction to the neutral particle detector while the remaining ions are bent into a Faraday cup. Figure taken from [16].

1 Surface barrier detector

A surface barrier detector consists of a n-type or p-type semiconductor material. By etching the surface and evaporating a thin gold or aluminum layer for electrical contact a depletion region comparable to other semiconductor detectors is created (Fig. 2.7).

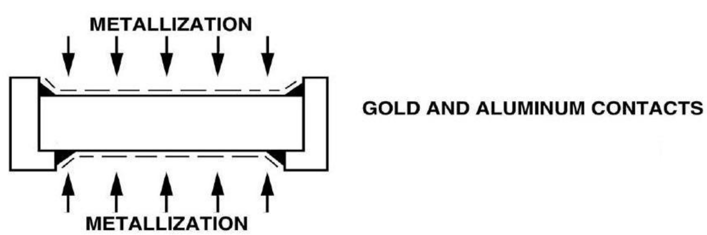

Figure 2.7: Simplified illustration of a surface barrier Si detector. Figure taken from [35].

Neutral atoms or molecules are ionized when they are interacting with matter as some of their electrons are stripped off. When the charged particles penetrate into the active region of the surface barrier detector free electron-hole pairs are produced and drift to the electrodes causing a signal proportional to the particle energy and the distance traveled. When the particle energy is just in the keV range the energy loss due to the surface dead layer of the detector can be significant and, thus, the particles can hardly reach the active region and no electron-hole pairs are produced. However, surface barrier detectors are still advantageous compared to other semiconductor detectors for low energy particles, since the energy loss caused by the surface layer is much smaller. [35–37]

2 Metallic magnetic microcalorimeter (MMC) detector

The main components of a metallic magnetic calorimeter (MMC) are an absorber, a paramagnetic sensor, and a heat sink. The sensor usually consists of a metal like gold doped with a paramagnetic material such as the rare earth metal erbium. The sensor has to be in good thermal contact with the absorber and spins inside the sensor material are aligned using a weak magnetic field. Also, the sensor is connected with a weak thermal link to the heat sink, which has a constant temperature in the range of millikelvin (Fig. 2.8).

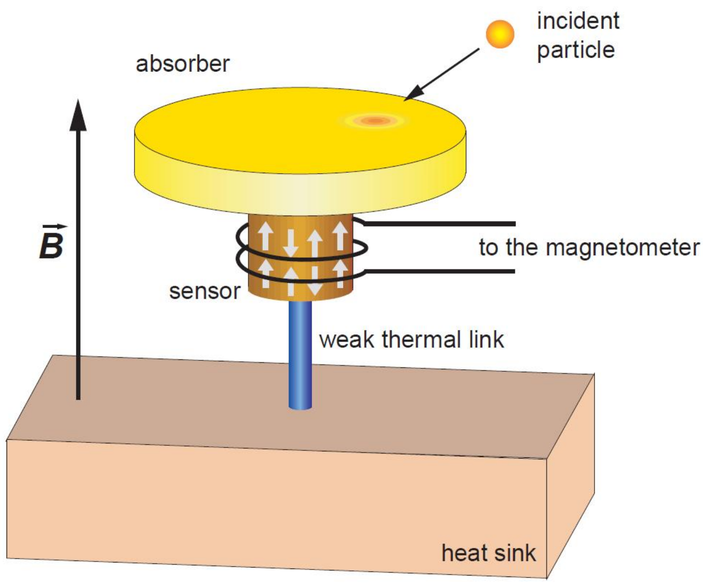

Figure 2.8: Detection principle of a metallic magnetic calorimeter (MMC) detector. The energy of an incoming particle impinging on the absorber of the detector is converted into heat, resulting in a warming of the absorber and the sensor. Due to the increase of the temperature the magnetization of the paramagnetic sensor changes which is measured using low-noise high bandwidth dc-SQUID magnetometers. Figure taken from [38].

The energy of an incoming particle impinging on the absorber of the detector is converted into heat, resulting in a warming of the absorber and the sensor. The change of the temperature δT is directly proportional to the particles energy δE:

$$\delta T = \frac{\delta E}{C_{tot}},$$

where C_{tot} is the total heat capacity of the sensor and the absorber.

Due to the increase of the temperature the magnetization M of the paramagnetic sensor changes according to:

$$\delta M = \frac{\partial M}{\partial T}\delta T = \frac{\partial M}{\partial T}\frac{\delta E}{C_{tot}}.$$

This change of magnetization δM is measured using low-noise high bandwidth dc-SQUID magnetometers [38, 39]. However, maximum count rates of MMC detectors are in the order of 1 kcps [40].

3 Particle detection via secondary electrons

This type of detector exploits the production of secondary electrons when primary particles impinge on a conversion element. The characteristics of the incoming particles are decisive for the applied conversion materials, as the production of secondary electrons depends on various factors such as particle energy, charge state, angle of incidence, structure, and treatment. The produced secondary electrons are detected using an electron multiplier, thus, every incoming particle generates an output pulse which can be amplified and counted. The setup of such a detector is advantageous for low energy particles, as no window is required and no dead layer exists. Hence, single particles of just some 100 eV can be detected. Besides, the output pulse of an electron multiplier has a width typically in the range of nanoseconds, i.e. detectors with a high time resolution can be realized. [41]

The neutral particle detector in the extended ILIAS setup (Fig. 2.6) has to be transparent for laser light, as it is positioned in the axis of the particle beam. Also, a high time resolution is needed, since the expected count rates are in the range of 10^5–10^6 cps depending on the current of the ion beam (see section 4.8). These requirements can only be fulfilled by a particle detector based on secondary electron emission using a glass plate with a thin and transparent conductive coating as conversion material. See the following chapter for a detailed description of the design and setup of the detector.

3 The Neutral Particle Detector

3.1 Principles

The objective was to construct a particle detector based on a conductively-coated glass plate to detect neutral particles produced in a laser photodetachment process. When the neutral particles hit the glass plate secondary electrons are ejected. Using suitable ion optics the emitted electrons are directed to a channel electron multiplier where they are detected (Fig. 3.1).

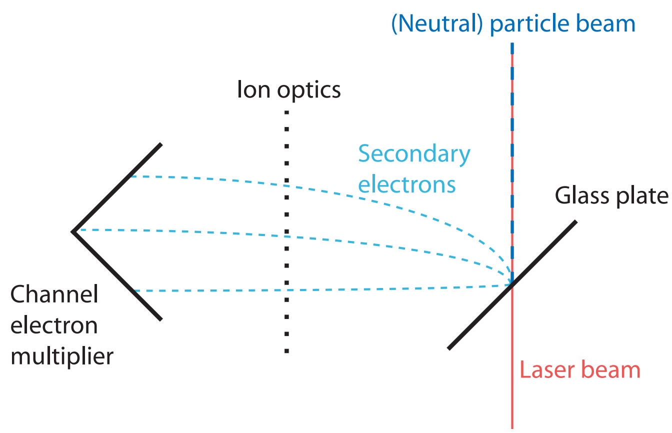

Figure 3.1: Schematic representation of the neutral particle detector. Neutral particles produced in a laser photodetachment process impinge on a conductively-coated glass plate which is transparent for laser light. The emitted secondary electrons are detected in a channel electron multiplier.

3.2 Components

3.2.1 The glass plate

The used glass plate is made of silicon oxid (quartz glass) coated with indium tin oxide. It has a square shape with a side length of 25 mm and the thickness is 1.1 mm. The surface resistivity is 70–100 Ω/sq and the transmittance for light is 86 % at 550 nm [42]. It is needed, since an ion- and a laser beam are eventually overlapped collinearly and therefore the detector has to be transparent for laser light. Since the neutral particles cannot be deflected by electric or magnetic fields it is necessary that the glass plate is located in the axis of the particle beam. It is mounted under a 45° angle with respect to the direction of the particle beam. This position is convenient insofar as the area of the glass plate orthogonal to the axis of the particle beam is maximized while the electrons are preferably emitted toward the channel electron multiplier. A bias voltage is applied to the coating of the glass plate to increase the number of emitted electrons.

3.2.2 Ion optics

The initial kinetic energy of the emitted electrons is approximately 5 eV [43] and thus negligibly small compared to typical voltages of an ion optical system. Therefore, the final kinetic energy of the electrons when they impinge on the surface of the channel electron multiplier (CEM) is determined only by the potential difference between the glass plate and the CEM. This should be chosen such that the emitted electrons have a kinetic energy between 10^2–10^3 eV to exploit the maximum detection efficiency of the CEM for electrons (Fig. 3.3(b)).

To make sure that the emitted electrons are focused into the channel electron multiplier an appropriate ion optical system was constructed and subsequently manufactured in our own workshop. It was ensured that the setup is as effective as possible, while effort and costs were kept low.

3.2.3 Channel electron multiplier (CEM)

A channel electron multiplier can detect charged particles, hard and soft X-rays, and ultraviolet radiation. The structure is made of ceramic and contains a curved channel which is coated with black lead glass [44] (Fig. 3.2(b)).

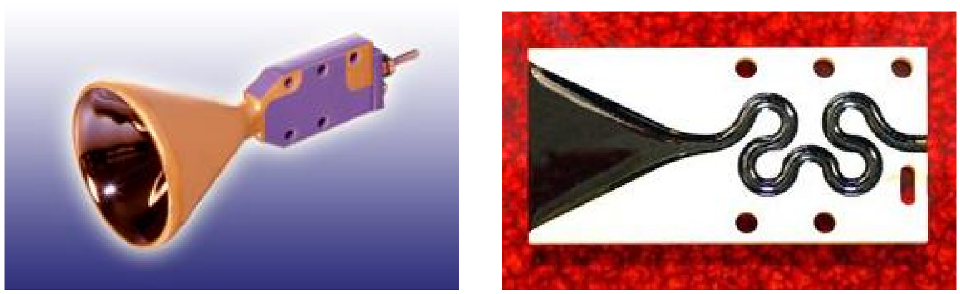

(a) Representative image of a standard channel electron multiplier.

(b) Cut view of a standard CEM (Type KBL210).

Figure 3.2: Images of standard CEMs. Figures taken from [44].

This surface has a high resistance and forms a continuous dynode when a voltage is applied between the input and the output end of the channel electron multiplier. When primary particles or photons impinge on the dynode secondary electrons are emitted, which are accelerated down the channel by the applied potential. These electrons produce further electrons by striking the surface, which leads to an avalanche process and a number of up to 10^8 secondary electrons per incident particle. The electron cloud is collected with an anode and produces a single pulse (Fig. 3.3(a)). The output pulse is easily detectable using a preamplifier, a discriminator, and a counter or rate meter. [44]

For the neutral particle detector a standard channel electron multiplier (Type KBL 20RS) by *Sjuts Optotechnik* [44] is applied to detect the emitted electrons from the glass plate. The

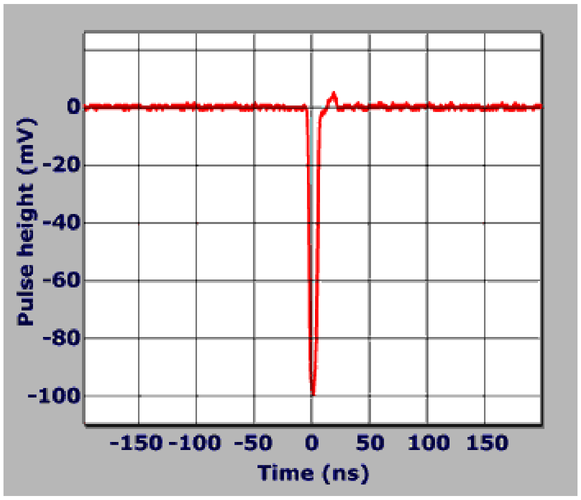

(a) Typical output pulse of a standard CEM at 2.5 kV applied voltage.

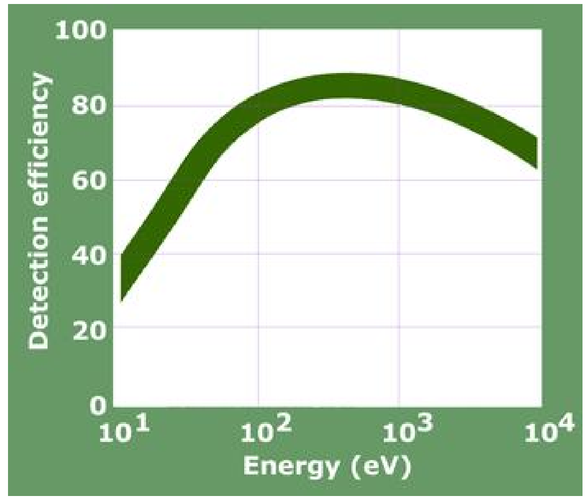

(b) Detection efficiency for electrons as a function of incident energy.

Figure 3.3: Characteristics of standard CEMs. Figures taken from [44].

used model has a round entrance funnel which measures 20 mm in diameter. Since the device is very delicate it was ensured that the CEM under no circumstances can be hit by the particle beam. The characteristics of this type of CEM are shown in Tab. 3.1. For the engineering drawing of the used CEM and for more plots in terms of the characteristics of standard CEMs see appendix A and B.

Typical gain at 2.3 kV applied voltage	10^8
Typical wall resistance	200 MΩ
Pulse height distribution at 2.6 kV and 3000 cps	$< 50\,\%$
Dark count rate above a threshold of –5 mV	< 0.02 cps
Maximum count rate	$5{\cdot}10^6$ cps
Typical pulse width (FWHM) at 2.3 kV	8 ns
Operating voltage	max. 3.5 kV
Temperature (operating and storage)	max. 70°C
Bake temperature in vacuum	max. 250°C

Table 3.1: Characteristics of standard CEMs. Table taken from [44].

3.3 Construction and design

3.3.1 Simulation with SIMION 8.0

Based on the mentioned requirements a holder for the glass plate and the appropriate ion optical system were designed by programing the geometry of the whole structure and simulating the trajectories of the emitted electrons using the simulation program SIMION 8.0 (Fig. 3.5). For the geometry file of the final design see appendix C.

It was ensured that the manufacturing process of the setup is simple and fast and that the whole structure consists of as few parts as possible. That led to a design, where the holder of the glass plate is part of the ion optical system. Additionally, the option to set parts of the ion optical system and the conductive coating of the glass plate on the same potential was explored in order to minimize the number of required electrical feedthroughs.

For the simulation of the trajectories of secondary electrons, the neutral particles were assumed to hit the glass plate centric and the direction of the ejected electrons was spatially uniformly distributed. Finally a design was found where the number of electrons reaching the entrance of the channel electron multiplier maximizes when a potential of –230 V is applied to the coating of the glass plate and the holder of the glass plate. By using a supplementary focus ring with an applied potential of 400 V it was achieved that 100 % of the simulated electrons from the glass plate reached the entrance of the CEM.

Since the detector is mounted in a vacuum chamber the simulation was finally repeated with a grounded housing enclosing the whole detector. It was found that this has no significant influence on the trajectories of the electrons.

Time resolution of the neutral particle detector

To determine the time resolution of the detector it was essential to know the time of flight (TOF) distribution of the secondary electrons from the glass plate to the entrance of the channel electron multiplier. For this purpose, a simulation with SIMION 8.0 with 10^5 electrons was performed and the result was illustrated in a histogram (Fig. 3.4). Assuming that one neutral particle impinges on the center of the glass plate – whereby more than one electron is emitted – the maximum time difference of the TOF of the electrons from the glass plate to the entrance of the CEM is 3 ns. It must be pointed out that the term time resolution in this context only refers to the maximum count rate of the detector but not to any delay of the detection of the particles, as this is irrelevant for the planned application.

In addition to the TOF distribution of the secondary electrons the time resolution of the detector depends on the output pulse width of the CEM, which is 8 ns (FWHM) (Tab. 3.1) and, thus, dominates the time resolution. For neutral particles impinging on the center of the glass plate the probability for double counting, i.e. that one neutral particle causes more than one output pulse of the CEM, is below 10^{-5} due to the relative wide output pulse of the CEM compared to the maximum TOF difference of 3 ns of the secondary electrons.

The influence of the dead time of the CEM on the count rate is estimated in the following: The measured count rate is assumed to be $r = 10^6$ cps and the dead time of the CEM is $\tau = 8$ ns. The real count rate is given by:

$$R = \frac{r}{1 - r\tau} = 1.008 \cdot 10^6 \, cps \tag{3.1}$$

Hence, the difference between the measured count rate and the real count rate due to the dead time of the CEM is less than 1 %.

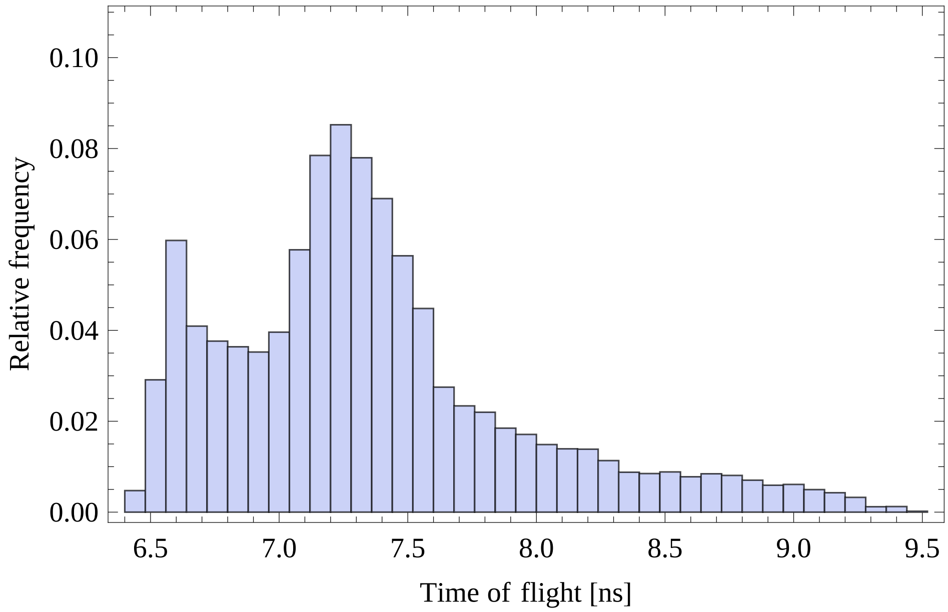

Figure 3.4: Histogram of the time of flight (TOF) of emitted secondary electrons due to one neutral particle impinging on the glass plate. The simulation was performed with SIMION 8.0 with 10^5 electrons and the neutral particle was assumed to impinge on the center of the glass plate and the direction of the electrons was uniformly distributed. The maximum time difference of the TOF of the electrons from the glass plate to the entrance of the CEM is 3 ns.

Summarizing, the time resolution is $<$10 ns and the maximum count rate of the detector is $5{\cdot}10^6$ cps (Tab. 3.1). For higher count rates the gain of the CEM dramatically decreases as illustrated in figure B.1(c). As the expected count rate of the photodetached ions is at least one order of magnitude lower than the maximum count rate of the detector the dead time of the CEM is negligible (equation 3.1). Thus, the detected count rate should correspond to the real count rate.

3.3.2 Setup and production

The detector is mounted in a 100CF six-way cross piece with an inner diameter of 100 mm. To ensure that all components fit into the intended vacuum chamber suitable holders were separately designed for the channel electron multiplier (Fig. 3.6(b)) and for the ion optical system, including the glass plate (Fig. 3.6(a)).

The separate holders ensure that the CEM can be installed in such a way that it cannot be hit by the particle beam and at the same time the glass plate can be moved out of the beam by a linear drive. All engineering drawings in this thesis have been plotted with the program *Solid Works 2010* [45].

Ion optical system and glass plate

The holder of the glass plate was manufactured from a standardized square pipe with a side length of 30 mm and the thickness is 2 mm. The glass plate is fixed with a thin shim made of spring steel. Thereby the glass plate can easily be replaced and at the same time the ion optical system and the coating of the glass plate are electrically connected (Fig. 3.7).

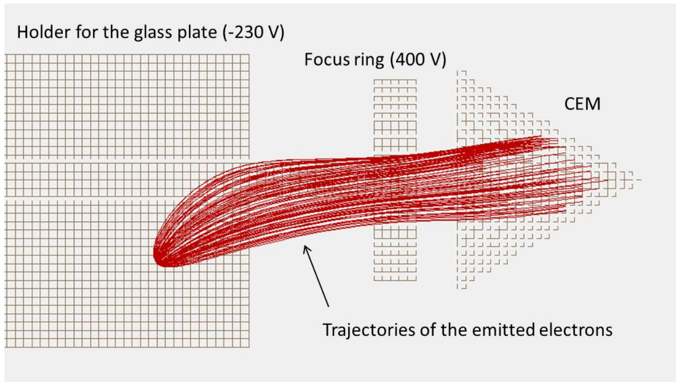

(a) xy-plane.

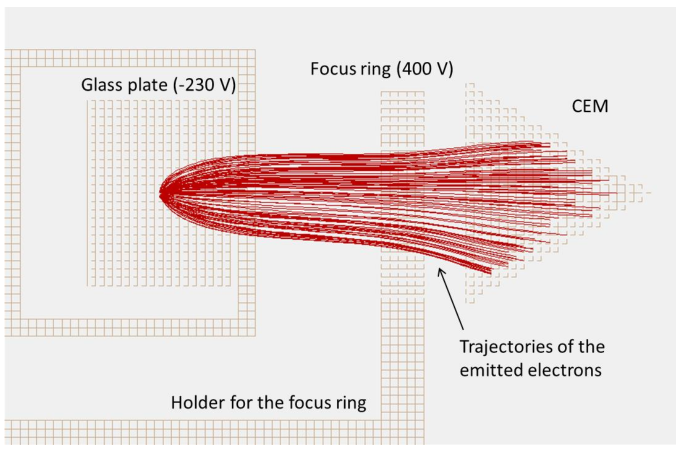

(b) xz-plane.

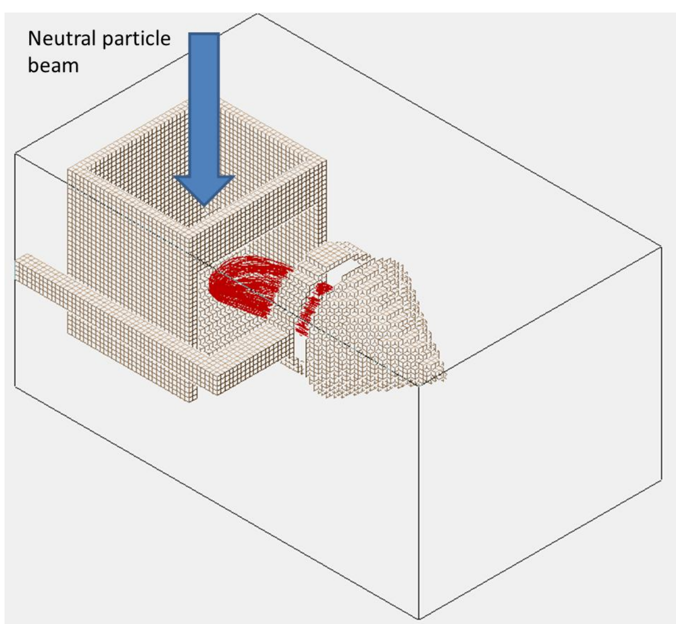

(c) 3D-view.

Figure 3.5: Final design of the neutral particle detector illustrated in SIMION 8.0. Due to particles impinging on the glass plate secondary electrons are emitted and guided to the entrance of the CEM using an appropriate ion optical system. The trajectories of the emitted electrons are represented in red.

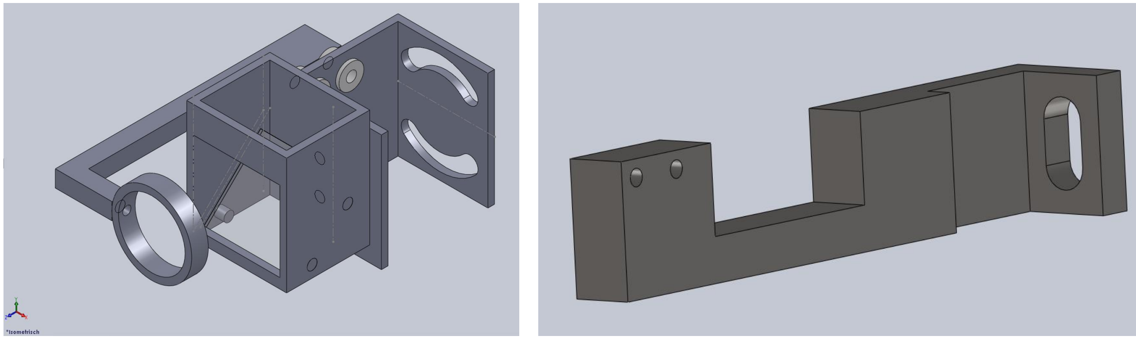

(a) Structure of the ion optical system and the holder for the glass plate.

(b) Holder for the channel electron multiplier.

Figure 3.6: Engineering drawings for the holders.

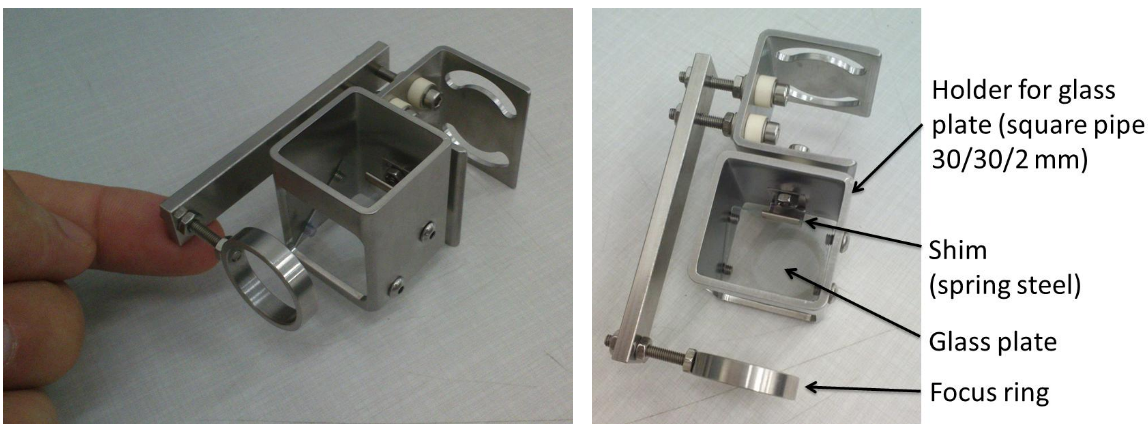

(a) Perspective 1

(b) Perspective 2

Figure 3.7: Holder for glass plate and ion optical system.

The holder of the glass plate and the ion optical system are mounted on a linear drive. In order not to restrict the flexibility of the structure metal springs are used for the electrical connections. Since the springs are made of a ferromagnetic material it was important to maximize the distance between the ion optical system and the springs. This was accomplished using a metal clip in order to prevent disturbance of the trajectories of the electrons by magnetic fields (Fig. 3.8).

Channel electron multiplier

The channel electron multiplier is mounted on a blank flange using the holder shown in Figure 3.6(b). The blank flange has two electrical feedthroughs (SHV) – one for the supply voltage and one for the output signal – which are electrically connected to the CEM using metal springs.

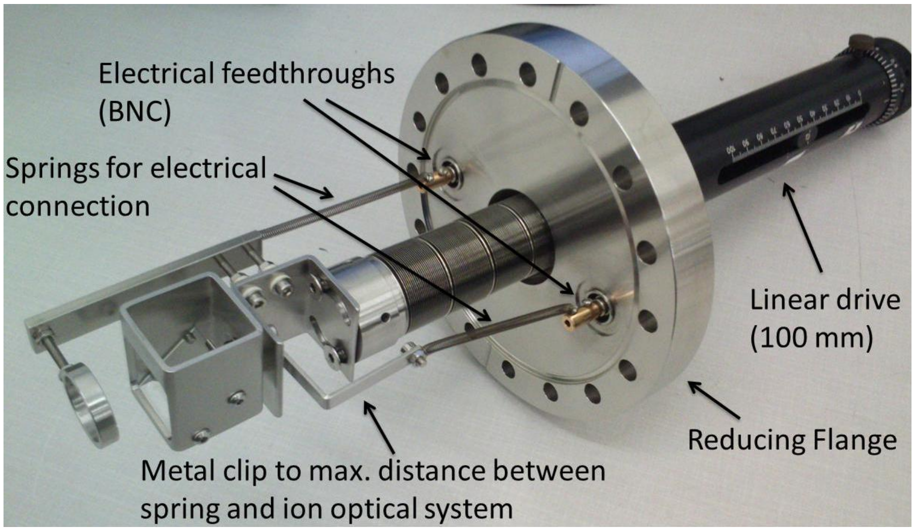

Figure 3.8: Coated glass plate and ion optical system mounted on a linear drive and a reducing flange.

The coated surface of the CEM has the characteristic of binding moisture, which causes a decrease in gain and leads to a reduction of the lifetime. To avoid this the CEM was unpacked, mounted, and stored in a glove box filled with argon.

The channel electron multiplier, the holder for the glass plate, and the ion optical system were finally installed in the 100CF six-way cross piece according to the construction developed with SIMION 8.0 (Fig. 3.10).

3.3.3 Electrical connections

Glass plate and ion optical system

The linear drive for the glass plate and the ion optical system is mounted on a reducing flange which has two BNC feedthroughs for the supply voltages. These are suitable for voltages up to 500 V and therefore fulfill the necessary requirements.

Channel electron multiplier

In operation a potential of around 2.5 kV has to be applied between the input and the output of the CEM to accelerate the secondary electrons down the channel. In addition it is advisable to apply a voltage of 100 V between the CEM output and the anode so that the electron cloud is accelerated out of the CEM toward the anode. This leads to a maximum gain and a narrow pulse height distribution. To implement the potential differences a circuit design recommended by the company *Sjuts Optotechnik* [44] was used (Fig. 3.11(a)).

Since the electronic components are not suitable for the ultra-high vacuum, the circuit was implemented in a small metal box outside of the vacuum chamber. The strong electric field caused by the high voltage in the signal cable can cause dark count rate [44]. To avoid this the metal box was positioned in close proximity to the vacuum feedthroughs to keep the cable length as short as possible (Fig. 3.11(b)).

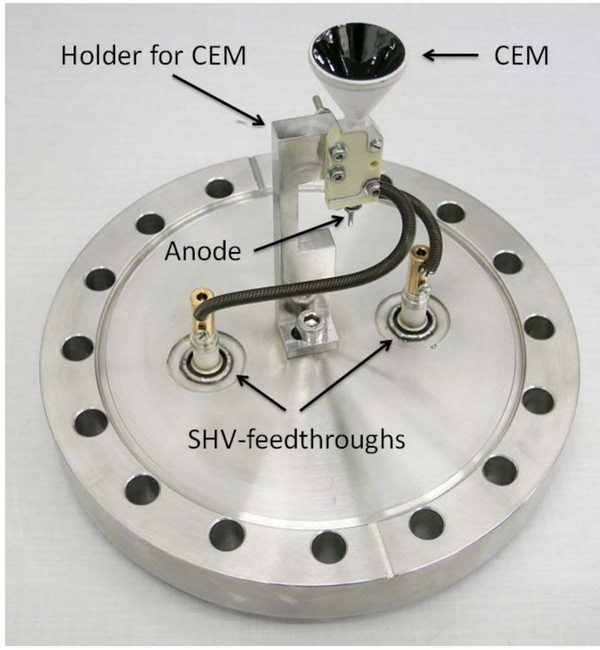

Figure 3.9: Channel electron multiplier mounted on a blank flange. The SHV-feedthroughs are connected to the anode and to the output of the CEM, respectively.

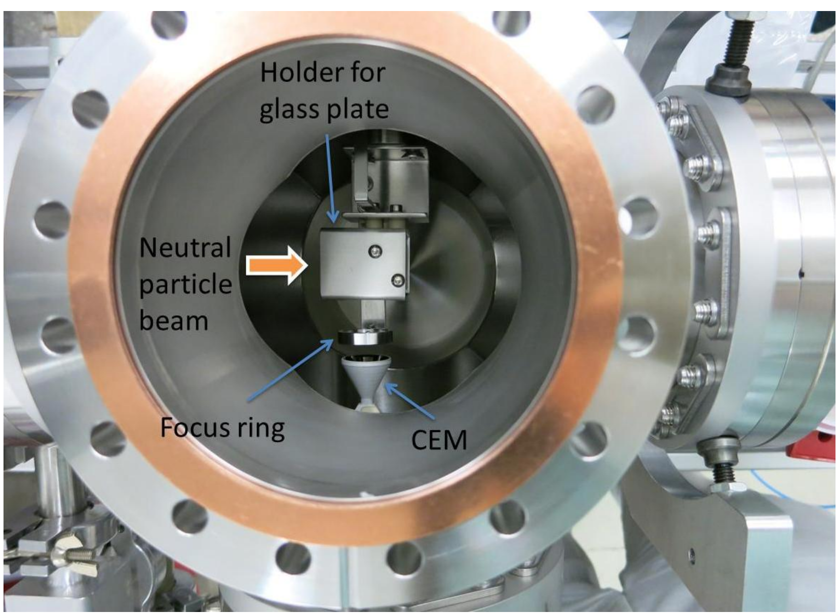

Figure 3.10: Channel electron multiplier, holder for glass plate, and ion optical system installed in six-way cross piece.

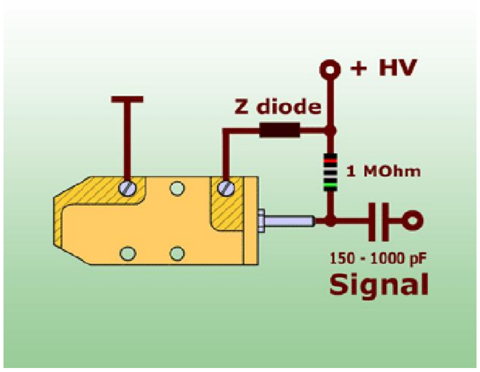

(a) Recommended circuit design to apply the required potentials to the CEM. Figure taken from [44].

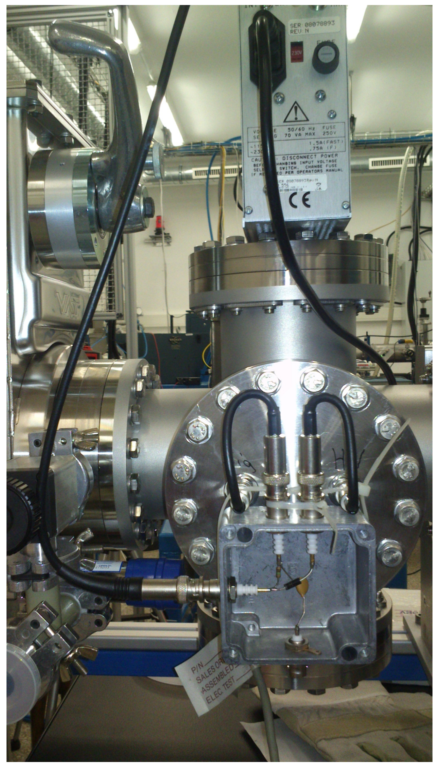

(b) For safety reasons the circuit is implemented in a grounded metal box as high voltage is applied to the CEM. Using cables the circuit is connected via SHV-feedthroughs to the CEM.

Figure 3.11: Wiring of the CEM.

4 Detection setup

The first functional test of the neutral particle detector described in the previous chapter was performed by investigating the photodetachment characteristics of $^{12}C^-$ and $^{12}CH^-$ ions. For this purpose the detector was embedded in the setup shown in figure 4.1.

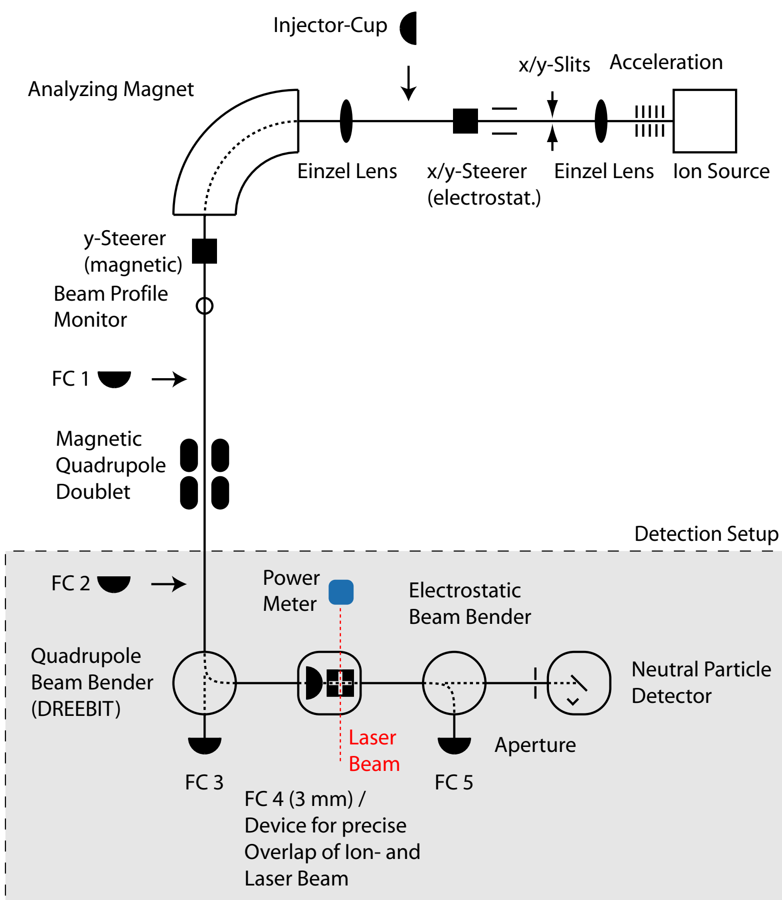

Figure 4.1: Schematic view of ILIAS and the detection setup. Main components: Cesium sputter ion source, analyzing magnet, magnetic quadrupole doublet, various Faraday cups (FC 1-5), 2 electrostatic beam benders, laser, device for precise overlap of the ion- and the laser beam, aperture to reduce background signal caused by electrons, neutral particle detector. The detection setup was designed in such a way that it can be used as probe region for the measurement of the efficiency of selective suppression described in section 2.4.

The detection setup was designed and installed in such a way that it can be used in a later phase of the project as the probe region for the measurement of the efficiency of selective suppression (Fig. 2.6) presented in section 2.4. However, in order to keep the first measurements simple the ion- and the laser beam were not overlapped collinear but perpendicular to each other. The main components of the setup will be described in detail in the following sections:

4.1 Negative ion beam spectrometer

For the mentioned photodetachment studies mass separated negative ion beams have to be provided. For this purpose a single cathode cesium sputter source is used which is capable of producing the wanted negative atomic and molecular ions and accelerates them to 16 keV. The mass separation is accomplished with an analyzing magnet. For detailed specifications of the functionality of the ion source and the analyzing magnet see section 2.3.1.

4.2 Magnetic quadrupole doublet

An ion beam passing through a quadrupole field is focused in x-direction while it is defocused in y-direction or vice versa. Two quadrupoles combined and rotated by an angle of 90° against each other (quadrupole doublet) yield a net focusing of the ion beam since the focusing effect predominates compared to the defocussing effect.

The magnetic quadrupole doublet in the measurement setup is needed to focus the ion beam sufficiently in order to maximize the transmission of the ions through the following quadrupole beam bender. At this stage of the project it operates as a placeholder for the gas-filled radio frequency quadrupole ion beam cooler (section 2.3.2), which will be installed in a later phase once the functional capability of the simplified setup is successfully tested.

4.3 Beam benders

There are two beam benders in the beam line. The first one is an electrostatic quadrupole beam bender by the German company *DREEBIT* [46] (Fig. 4.2) and the second one is an electrostatic beam bender developed and manufactured by the research group of Isotope Research and Nuclear Physics at the University of Vienna.

The *DREEBIT* quadrupole beam bender has 4 equal electrodes which are shaped as quarter pipes. The electrodes are set on the same potential with alternating polarities and their arrangement forms a typical quadrupole. Assuming a negatively charged particle beam, the ions are attracted by the positive electrodes and repelled by the negative electrodes. In this way the ions are directed through the electrostatic quadrupole field. The beam bender is capable of bending ion beams in charge state q with energies up to $30 \cdot \mathrm{q}$ keV by an angle of 90° [47] (Fig. 4.3).

The in-house developed beam bender has also 4 electrodes, but they do not form a quadrupole. Two electrodes with opposite polarity are arranged in a grounded metal pipe, respectively, and generate an electric field by applying a defined voltage to the electrodes. The particle beam enters the pipes through slits and the ions are deflected by an angle of

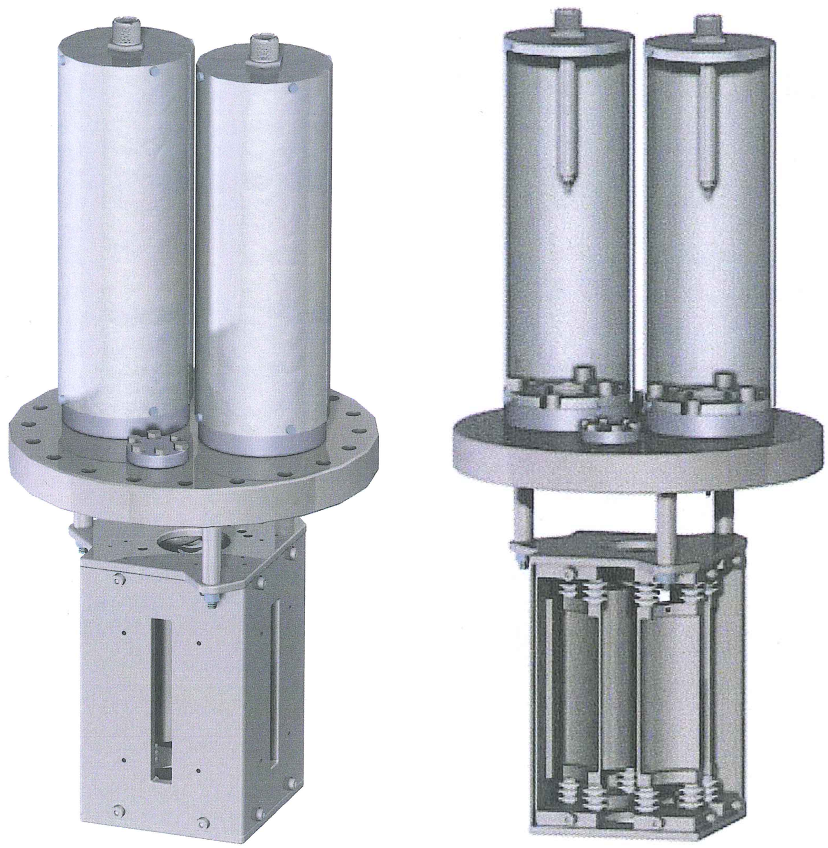

(a) Electrostatic quadrupole beam bender mounted on a standard CF160 flange.

(b) Cut view of the electrostatic quadrupole beam bender.

Figure 4.2: Quadrupole beam bender by *DREEBIT*. The overall height is 448 mm. The electrical feedthroughs are shielded with two high voltage covers. The beam bender is capable of bending ion beams in charge state q with energies up to $30 \cdot$ q keV by an angle of $90°$. Figures taken from [47].

$45°$ in each case. Hence, the charged particles are bent by an angle of $90°$ in total. Neutral particles can exit the beam bender in a straight direction through different slits (Fig. 4.4). To bend an ion beam with a kinetic energy of 16 keV the potential configuration of the electrodes is approximately ± 13 kV (Fig. 4.5).

For the functional test of the neutral particle detector the first beam bender in the beam line (Fig. 4.1) is needed to separate neutral particles produced due to electron loss processes occurring in collisions between the ion beam and the residual gas (and in the future by photodetachment in the ion cooler, respectively) and to deflect the ion beam in the detection setup. The second beam bender separates neutral particles produced in the laser photodetachment process of the probe laser from the ion beam. Thus, the ion beam current is measured with an off-axis Faraday cup (FC 5) while the produced neutrals move on in straight direction to the neutral particle detector.

As soon as the radio frequency quadrupole ion cooler is installed in the setup instead of the

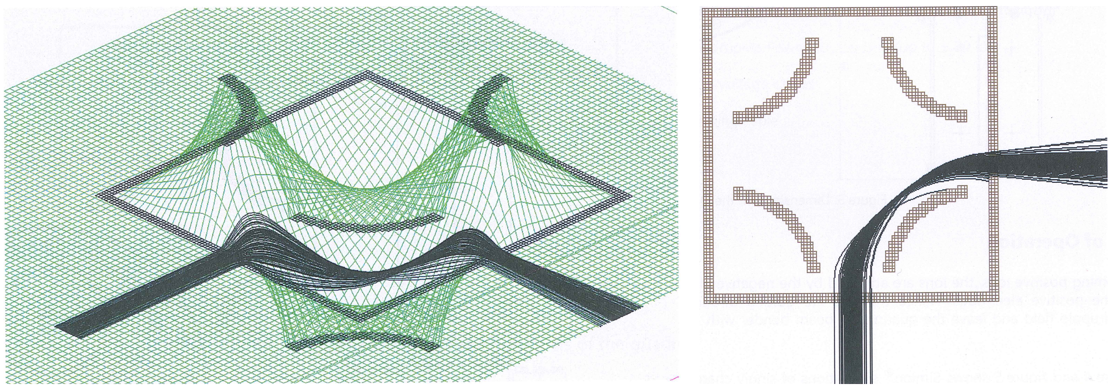

(a) Simulation of the beam geometry in the in the quadrupole beam bender (3D-view).

(b) Simulation of the beam geometry in the in the quadrupole beam bender (top view).

Figure 4.3: Simulation of the beam geometry in the quadrupole beam bender with singly charged argon ions with SIMION. The applied voltage of the electrodes is $\pm 26\,\mathrm{kV}$. Figures taken from [47].

quadruple doublet the two beam benders are required for the measurement of the efficiency of selective suppression described in section 2.4.

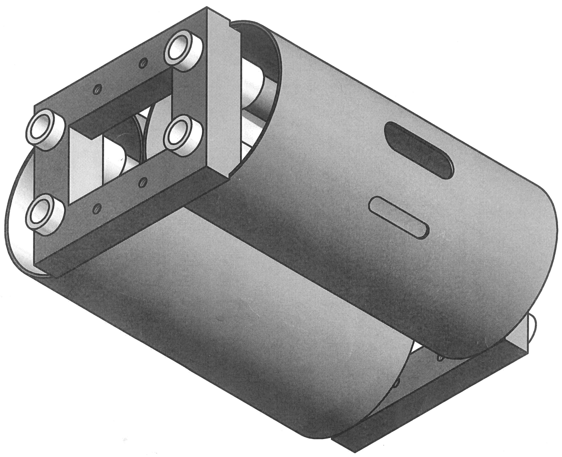

(a) In-house developed and manufactured beam bender (3D-view).

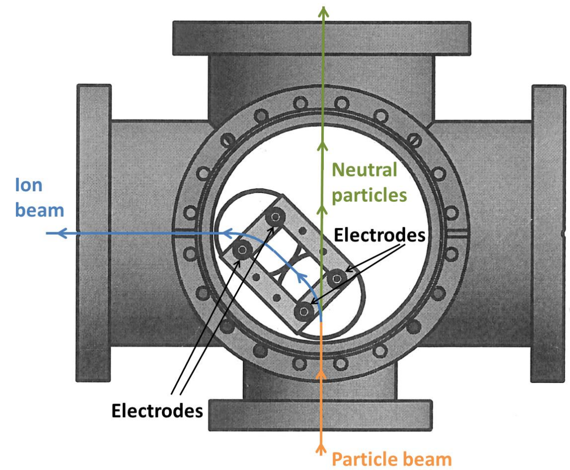

(b) Beam bender in 100CF 6-way cross piece.

Figure 4.4: In-house developed and manufactured beam bender. The charged particles are guided through two separated electrical fields generated by two electrodes, respectively. By this the ion beam is deflected in total by an angle of 90°. Neutral particles exit the bender in straight direction.

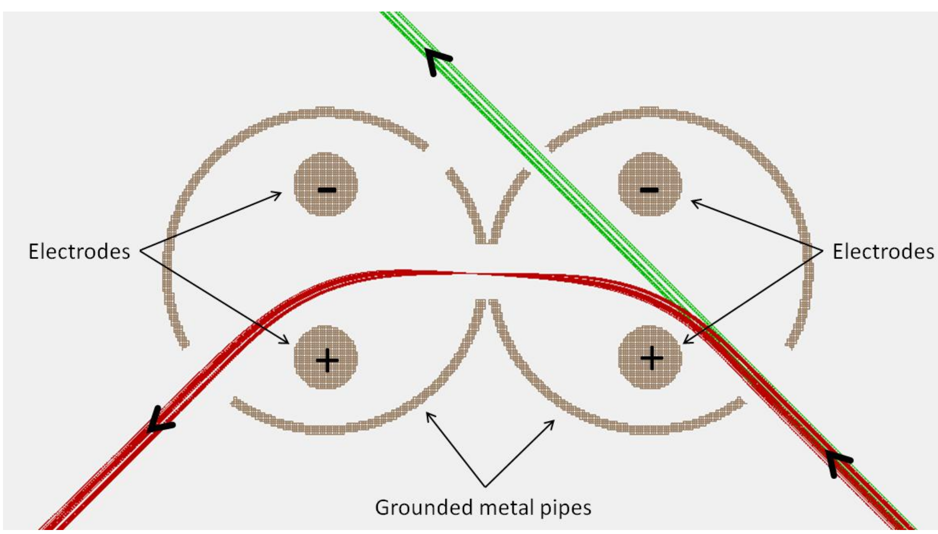

Figure 4.5: Simulation of the beam geometry in the in-house developed beam bender with SIMION. The simulation was performed with a 16 keV $^{12}C^{-}$ ion beam (illustrated in red) and a neutral particle beam (illustrated in green), respectively. The potential applied to the electrodes is ± 13 kV.

4.4 Device for precise overlap of ion- and laser beam

As mentioned before the ion- and the laser beam were overlapped perpendicular to each other in order to keep the setup of the first tests as simple as possible. For this purpose a device was designed that ensures a precise overlap of the beams. It was manufactured from a metal block with a square base area whose side length was 25 mm. The block has two holes of 3 mm in diameter, one for the ion beam and one for the laser beam, which cross in the center of the device. Since secondary electrons might be ejected when particles impinge on the metal surface the block is hollowed in order to minimize possible interactions and the resulting background signal. In addition, this layout is advantageous for precise tuning of the laser beam, since the beam can only pass through the entrance and the exit hole if it is perfectly arranged, as no wall reflections are possible.

The device for precise overlap of ion- and laser beam is combined with a Faraday cup with an inlet aperture which measures also 3 mm in diameter. The vertical distance between the inlet of the Faraday cup and the holes of the device for precise overlap of ion- and laser beam is approximately 40 mm. This coupled setup is mounted on a linear drive and, thus, enables the measurement of the current of the ion beam right at the point where the laser beam and the ions are interacting. Figure 4.6 shows the final setup of the device for precise overlap combined with a Faraday cup.

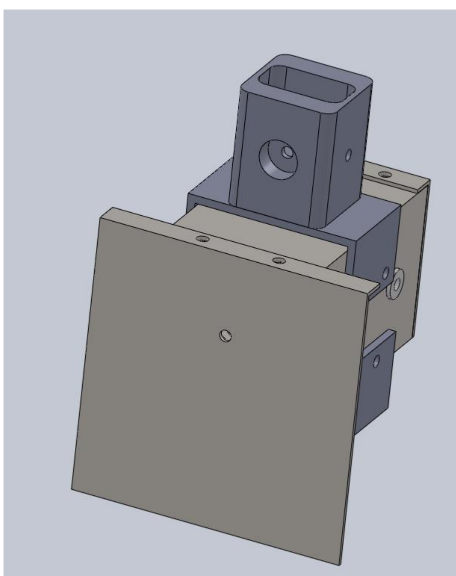

(a) Engineering drawing of the setup.

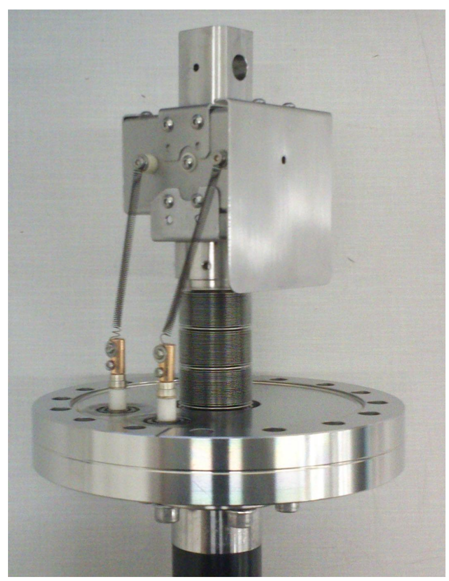

(b) Setup mounted on linear drive.

Figure 4.6: Device for precise overlap of ion- and laser beam combined with a Faraday cup. The inlet of the Faraday cup and the holes of the device for precise overlap of ion- and laser beam measure 3 mm in diameter, respectively, and the vertical distance is approximately 40 mm. The device is hollowed in order to minimize interactions between the ions and the metal block, as this could produce secondary electrons and, thus, the background signal would increase. Besides, precise tuning of the laser beam is easier, since the beam can only pass through the entrance and the exit hole if it is perfectly arranged.

4.5 Laser

The used laser is an infra red laser by the Chinese company *Changchun New Industries Optoelectronics Technology Co., Ltd.* [48]. The output power of the laser is approximately 13 W and the wavelength is adjustable in the range between 970 nm and 990 nm by the temperature of the laser system (Fig. 4.7). The corresponding energy range of the photons is between 1.253–1.279 eV i.e. the C^- and the CH^- anions ($EA(C^-) = 1.262$ eV, $EA(CH^-) = 1.238$ eV) to be investigated (see section 2.2.1) can be neutralized by this laser.

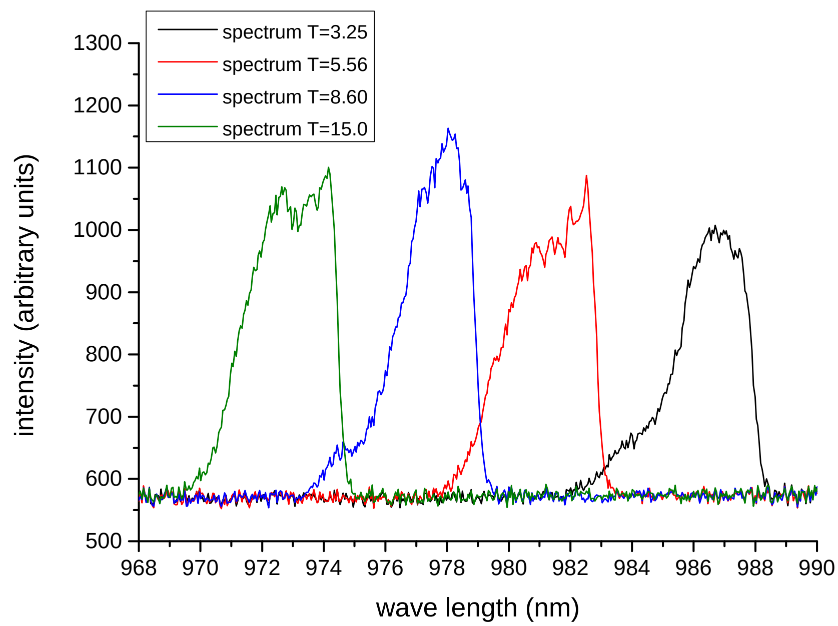

Figure 4.7: Influence of the temperature of the laser system on the light spectra. The wavelength is adjustable in the range between 970 nm and 990 nm.

The laser beam is focused on the point where it is overlapped with the ion beam using focusing optics composed of a concave lens (f = –50 mm), a convex lens (f = 200 mm), and two mirrors. The setup is represented in figure 4.8. A power meter placed on the opposite side of the six-way cross piece is used to find the optimal tuning of the mirrors for maximum transmittance of the laser beam.

As parts of the setup could heat up by absorption of laser light the power dissipation of the laser beam due to the entrance and the exit window of the vacuum chamber was investigated. For this purpose an additional window was placed under a ~20° angle in the laser beam between the second mirror in the optical path and the entrance window. The power of the transmitted and of the reflected laser beam was detected simultaneously using an extra power meter. Subsequently the measurement was repeated without the additional window. It turned out that almost the total power dissipation of the laser beam is induced by reflection and, thus, the windows cannot heat up appreciably (Tab. 4.1).

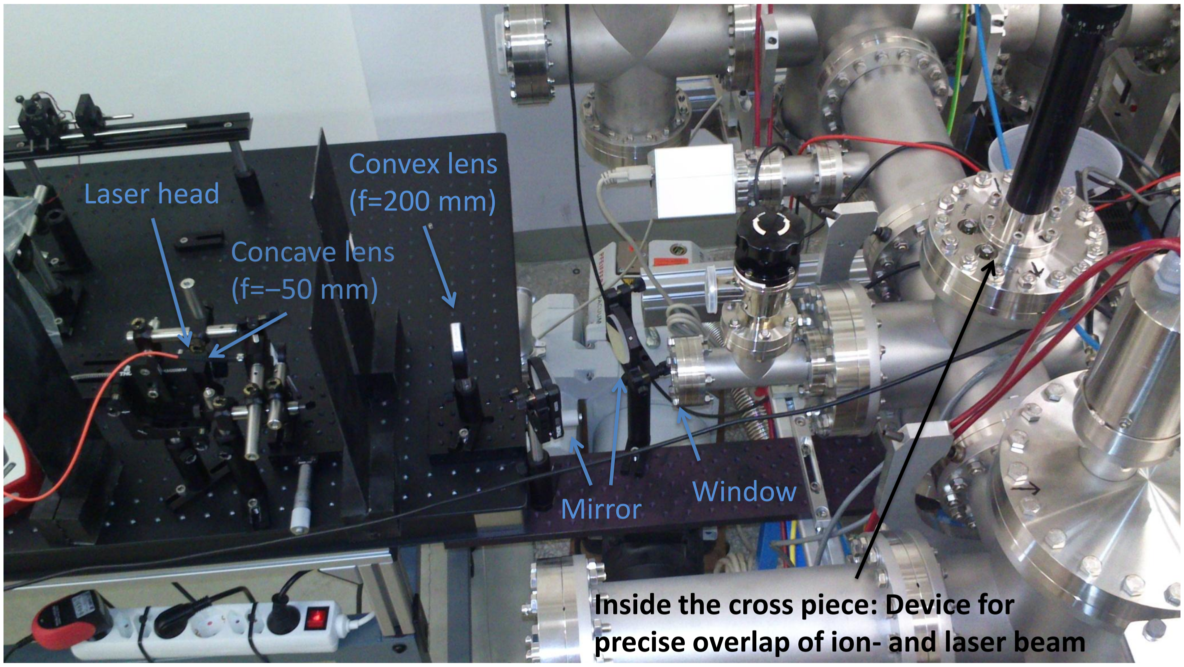

Figure 4.8: Setup of the laser. The laser beam is focused by a concave lens (f = –50 mm) and a convex lens (f = 200 mm) and directed through the device using two mirrors. A power meter located on the opposite side of the cross piece is used to find the optimal tuning of the mirrors for maximum transmittance of the laser beam.

Additional window	$P_{transmitted}$ [W]	$P_{reflected}$ [W]
in	10.2	0.99
out	11.2	0

Table 4.1: Measurement of the power dissipation of the laser beam due to the entrance and the exit window of the vacuum chamber. The total power dissipation of the laser beam is induced by reflection, thus, the windows of the vacuum chamber cannot heat up appreciably.

4.6 Signal processing (neutral particle detector)

The setup and the operating mode of the neutral particle detector have already been described in detail in chapter 3. The signal processing of the neutral particle detector was implemented by converting the output pulse of the channel electron multiplier (CEM) using a preamplifier/discriminator, a single channel analyzer, and a rate meter connected to a computer system (Fig. 4.9):

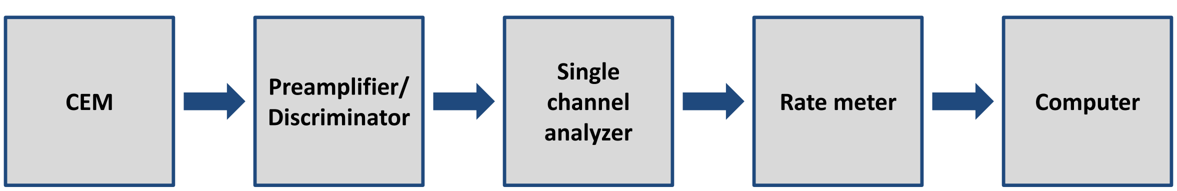

Figure 4.9: The output pulse of the CEM was processed using a preamplifier/discriminator, a single channel analyzer, and a rate meter connected to a computer system.

- Preamplifier/discriminator
  The used preamplifier/discriminator PAD01A by *WMT-Elektronik GmbH* (Fig. 4.10) is designed for amplifying typical output pulses of channel electron multipliers or photo multiplier tubes and converting the pulses into a rectangular signal. For high count rates dead time and output pulse width deviate up to $\pm 20\,\%$, thus, the preamplifier/discriminator is appropriate for cases with expected count rates not higher than some 10^5 cps [44]. For detailed listing of the characteristics of the preamplifier see appendix E.

Figure 4.10: Representative image of the used preamplifier/discriminator for the output signal of the CEM. Figure taken from [44].

- Single channel analyzer and rate meter
  As the output signal of the preamplifier/discriminator was slightly deformed due to reflections in the cable the single channel analyzer 552 PSA/T-SCA by *Ortec* was used to convert the signal into a rectangular signal. An upper and lower threshold can be adjusted in such a way that a possible disturbance or electronic noise is not detected. For the photodetachment measurements described in the next chapter the lower threshold was set to around 350 mV and the upper threshold was set to 10 V.

  The frequency of the resulting rectangular signal was measured using the rate meter *Ortec 441*, which was connected to a computer system where the measured count rate was directly displayed and plotted. For very low count rates such as the dark count rate of the CEM a counter was used instead of the rate meter.

4.7 Aperture to reduce background signal

In this section the background signal caused by neutral particles produced via electron loss processes occurring in collisions between the ions and the residual gas will be estimated:

- Estimation of the particle density of the residual gas using the ideal gas equation:

$$p \cdot V = n \cdot R_m \cdot T$$

$$R_m = R_s \cdot M$$

Since the residual gas is air the corresponding values for the specific gas constant $R_{s,air} \cong 287 \frac{J}{kg \cdot K}$ and the molar mass $M_{air} \cong 29 \cdot 10^{-3} \frac{kg}{mol}$ are inserted into the ideal gas equation. The pressure is $p = 5 \cdot 10^{-8}$ mbar and the temperature is 293 K. This yields for the molar amount per volume:

$$\frac{n}{V} \cong 2 \cdot 10^{-9} \frac{mol}{m^3}$$

And thus for the particle density:

$$\rho = \frac{n}{V} \cdot N_A \cong 10^{15} \frac{\#}{m^3}$$

- Estimation of the detachment factor due to the interaction of the ions with residual gas: The detachment factor is given by

  $$D(x) = 1 - e^{-\rho \cdot \sigma \cdot x}$$

  The interaction zone between the two electrostatic beam benders (Fig. 4.1) is approximately 1 m and the cross section for electron detachment due to collisions with N_2 for C_n^- and C_nH^- (n=1, 2) is $\sigma = 10^{-15}$ cm^2 [49]. This yields:

  $$D \cong 1 \cdot 10^{-4}$$

- Estimation of neutralized particles:

  Assuming an ion beam of 1 nA ($\widehat{=} 6 \cdot 10^9 \frac{ions}{s}$) yields for the number of neutralized particles:

  $$D \cdot 6 \cdot 10^9 \frac{\text{ions}}{\text{s}} \cong 6 \cdot 10^5 \frac{\text{neutrals}}{\text{s} \cdot \text{m}} \tag{4.1}$$

First measurements with a 16 keV $^{12}C^-$ ion beam of some nA tuned to FC 5 showed a background signal in the order of 10^6 cps which corresponds to the estimated count rate. However, the detected background signal was still around 10^5 cps when the ion beam was tuned to FC 4 and, thus, the direct beam path to the detector was blocked. In addition the signal depended strongly on the ion beam tuning. Hence, a relevant fraction of the background signal seemed to be caused by secondary electrons ejected due to interaction of particles with matter of various devices in the beamline. However, it is not clear how they could pass the second beam bender and hit the glass plate and the CEM, respectively.

The measured count rate of the CEM when no ion beam is tuned to the detection setup, is approximately 2–3 cps. This result is around two orders of magnitude higher than the dark count rate specified by the manufacturing company (Tab. 3.1). Besides, the count rate increases by an order of magnitude when the nearby vacuum gauge is on, due to electron emission.

Hence, the total background signal is caused by neutralized ions due to collisional detachment of the electron, secondary electrons ejected due to interaction of particles with matter, and to a small extent also electron emission of the vacuum gauge.

In order to reduce the background signal caused by (secondary) electrons an appropriate aperture was constructed (Fig. 4.11). It has an outer diameter of 97 mm and a drill hole which measures 10 mm in diameter. The aperture was installed in front of the neutral particle detector and a negative potential of –230 V was applied. The distance of around 10 cm between the aperture and the detector ensures that the potential applied to the aperture does not influence the trajectories of the secondary electrons ejected from the coating of the glass plate. In this way, both a mechanical and an electrostatic shielding was implemented, resulting in a reduction of the background signal caused by the vacuum gauge by two orders of magnitude (Tab. 4.2). However, the total background signal when the ion beam was tuned to FC 5 was just slightly lowered.

Aperture \ Vacuum gauge	on	off
in	0.5	0.1
out	25.0	2.5

Table 4.2: Count rate of the channel electron multiplier [cps] for different cases when no ion beam is tuned to the detection setup: Aperture installed/not installed, vacuum gauge on/off.

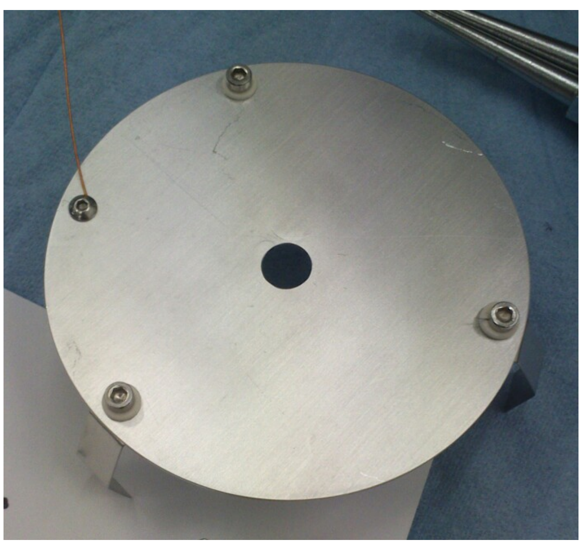

Figure 4.11: Aperture to reduce background signal caused by electrons. A voltage of –230 V is applied to the aperture to repel secondary electrons produced by interaction of the ion beam with matter in the vacuum chamber and electrons produced in the vacuum gauge.

Despite the shielding the count rate was still in the range of 10^6 cps when the ion beam of some nA was tuned to FC 5. Thus, the tuning of the ion beam, the influence of the applied voltages to the ion optics of the neutral particle detector, the correlation to the current of the ion beam, and the influence of the vacuum were analyzed. It turned out that the background signal depends strongly on the quality of the ion beam tuning and that it is proportional to the current of the ion beam. Especially at the first beam bender the characteristics of the ion beam seem to be crucial. This correlation requires further investigations, since electrons produced in the bender due to particles impinging on the electrodes should not be able to reach the neutral particle detector, as mentioned before. Also, the background signal caused by collisional detachment depends strongly on the vacuum in the detection setup (Tab. 4.3).

Vacuum [mbar]	Count rate [kcps/nA]
$3.5{\cdot}10^{-8}$	80
$3.8{\cdot}10^{-8}$	86
$6.6{\cdot}10^{-8}$	125

Table 4.3: Count rate per nA of the neutral particle detector as a function of the vacuum. The background signal caused by collisional detachment depends strongly to the vacuum.

Using slits (Fig. 4.1) to minimize the beam width and careful tuning enabled the reduction of the background signal of a 16 keV $^{12}C^-$ ion beam of ~280 pA to around 25000 cps, i.e. <100 cps/pA. Thus, the background signal was clearly lower than the estimated value of around 600 cps/pA (Equ. 4.1). This could be attributed to various reasons:

1. The vacuum was measured at one point of the detection setup only, thus, the value for the vacuum in the axis of the ion beam could have differed from the value assumed for the estimation.
2. Ions neutralized by collisional detachment could have been scattered and, thus, could not have reached the detector.
3. The cross section for collisional detachment for $^{12}C^-$ ions given in [49] could be wrong.

It was additionally found out that the highest count rate is measured when the voltage applied to the focus ring is zero (Tab. 4.4). This seems to be contrary to the corresponding

Focus ring [V]	Glass plate [V]	Count rate [cps]
–300	0	200
–300	–250	300
–300	–300	15 000
–300	–400	16 000
0	0	11 000
0	–40	17 000
0	–240	17 500
400	–240	9000
400	–440	14 000

Table 4.4: Count rate of the neutral particle detector as a function of the applied voltage to the focus ring and the coating of the glass plate. The $^{12}C^-$ ion beam of 150 pA was tuned to FC 5.

simulations in SIMION 8.0 described in section 3.3.1. However, a positive potential close to the entrance of the channel electron multiplier apparently attracts secondary electrons ejected from its surface. Thus, the loss due to the mentioned effect is greater than the benefit by a better focusing of the secondary electrons from the glass plate. Variation of the voltage applied to the glass plate between –40 and –240 V – when the voltage applied to the focus ring was zero – had only little influence. After all the focus ring can be used as an analyzing tool to investigate the characteristics of the background signal and the origin of the detected particles. A potential of –300 V applied to the focus ring of the detector (Fig.

3.7(b)) prevents ejected electrons from the glass plate to reach the entrance of the CEM. The resulting count rate of just 300 cps (Tab. 4.4) in the presence of a 150 pA $^{12}C^{-}$ ion beam suggests that the main part of the background signal is caused by secondary electrons ejected from the glass plate due to neutral particles impinging on the conductive coating.

A 16 keV $^{12}CH^{-}$ molecular ion beam causes a background signal of ~600 cps/pA which is much higher than that of $^{12}C^{-}$ ions. Although this background count rate corresponds fine to the estimated value (Equ. 4.1), these findings conflict with the results from Nascimento et al. [49], who measured the collisional detachment cross sections of $^{12}C^{-}$ and $^{12}CH^{-}$ to be almost the same. One reason for a higher count rate compared to the $^{12}C^{-}$ ions could be that neutralization by collision with residual gas atoms is enhanced due to molecular excited states. However this requires further investigation. In practice, this means that for the experiments with $^{12}CH^{-}$ the ion beam current has to be sufficiently lowered to obtain roughly the same background signal and not to overload the CEM.

4.8 Estimation of the count rate of photodetached ions

For this estimation a $^{12}C^{-}$ ion beam with an energy of 16 keV was considered.

The detachment factor f is given by the following:

$$f = 1 - e^{-\phi\sigma t}.$$

The photodetachment cross section σ is assumed to be $\sigma = 10^{-17}\,\mathrm{cm}^2$ [50]. The photon flux ϕ of the used laser with a laser power of $P = 13\,\mathrm{W}$, a wave length of $\lambda = 975\,\mathrm{nm}$, and a beam diameter of $d = 3\,\mathrm{mm}$ is

$$\phi = \frac{P \cdot \lambda}{A \cdot h \cdot c} = 9 \cdot 10^{24} \frac{1}{m^2 s},$$

where A is the sectional area of the laser beam, h is the Planck constant in eV·s, and c is the speed of light.

The velocity of ^{12}C particles with an energy of 16 keV is

$$E = \frac{1}{2} m v^2 \Rightarrow v = \sqrt{\frac{2E}{m[eV]}} \cdot c = 5 \cdot 10^5 \frac{m}{s}$$

and, thus, the interaction time between laser beam and ion beam is

$$t \approx 6\,ns.$$

Hence, the detachment factor is

$$f = 1 - e^{-\phi\sigma t} \approx 5.4 \cdot 10^{-5}$$

At a current of the ion beam of 1 nA ($\widehat{=}\, 6 \cdot 10^9\, \frac{\mathrm{ions}}{\mathrm{s}}$) approximately $3 \cdot 10^5\, \frac{\mathrm{ions}}{\mathrm{s}}$ are neutralized by laser photodetachment.

Based on the estimation of the background signal caused by neutral particles produced via electron loss processes occurring in collisions between the ions and the residual gas and the estimation of the number of neutralized particles via laser photodetachment one can expect that the count rate of the detected neutral particles increases by approximately 50 % when the laser is on.

5 Measurements and results

As mentioned before, the neutralization of an atomic and a molecular anion ($^{12}C^{-}$ and $^{12}CH^{-}$) via laser photodetachment was investigated using the detection setup described in the previous chapter. For clear and demonstrative presentation of the test results the following parameters were automatically logged and plotted:

- Current of the ion beam
  As the detachment rate depends – besides the ion laser interaction time and the photodetachment cross section – on the flux density of the ions (section 4.8) the current of the ion beam was measured with FC 5 which is placed after the second beam bender (Fig. 4.1) in order to detect possible fluctuations.

- Power of the laser beam
  The transmitted power of the laser beam was measured by a power meter placed on the opposite side of the beam line (Fig. 4.1 and 4.8). A power-proportional output voltage was recorded by the data acquisition system. In the following plots, this voltage signal is only given in arbitrary units to qualitatively illustrate whether the laser was on or off. The corresponding data points in the plots are not correlated to the real laser power.

- Count rate
  The amplified output signal of the neutral particle detector was converted into a rectangular signal and logged using a rate meter connected to the computer system (section 4.6).

5.1 $^{12}C^{-}$

The photodetachment studies with $^{12}C^{-}$ were carried out with a 16 keV ion beam of approximately 300 pA. After careful beam tuning to FC 5 the background signal was ~25000 cps. Since the laser wavelength was set to $\lambda = 986$ nm ($\widehat{=}$ 1.258 eV) at the beginning and the electron affinity (EA) of $^{12}C^{-}$ is 1.262 eV (section 2.2.1) no ions were neutralized via laser photodetachment, hence, no increase of the count rate was detected when the laser was on (Fig. 5.1(a)).

When the laser wavelength was set to $\lambda = 982$ nm ($\widehat{=}$ 1.263 eV) one could already observe a slight difference of the output signal of the detector when the laser is on and off, respectively (Fig. 5.1(b)). Further reduction of the wavelength to $\lambda = 978$ nm ($\widehat{=}$ 1.269 eV) and $\lambda = 973$ nm ($\widehat{=}$ 1.275 eV) yields a considerable increase of the count rate when the laser is on (Fig. 5.1(c), 5.1(d)).

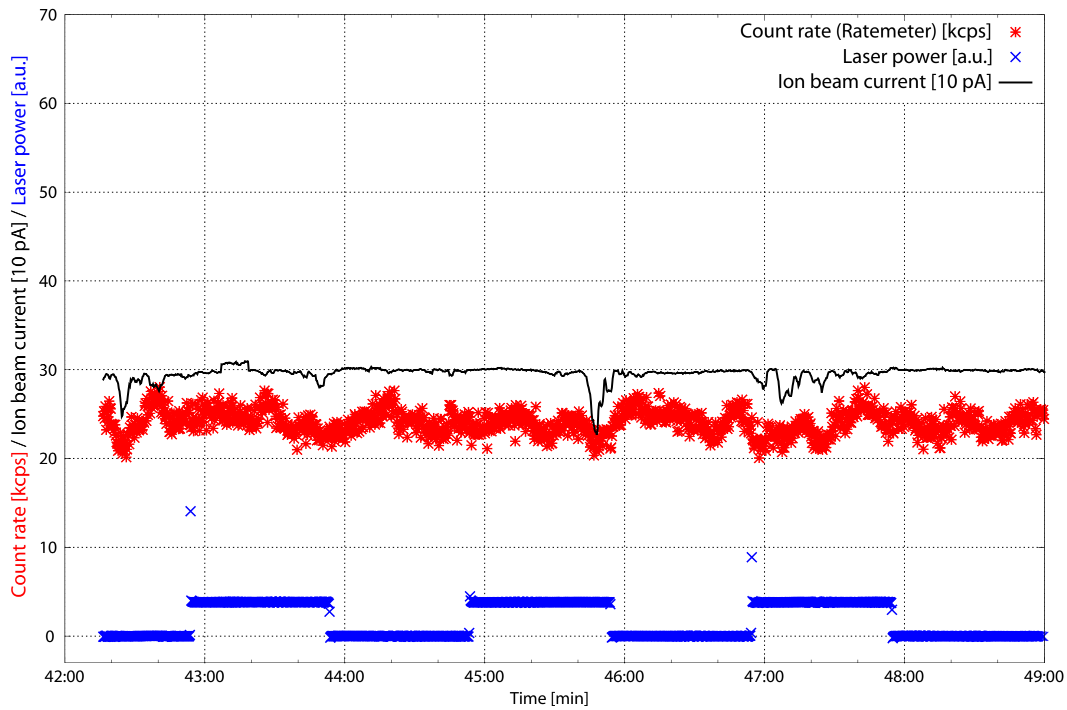

(a) Laser wavelength: $\lambda = 986\,\text{nm}$ ($\widehat{=}\, 1.258\,\text{eV}$). No increase of the signal is observed as the EA of $^{12}C^-$ ions is $1.262\,\text{eV}$.

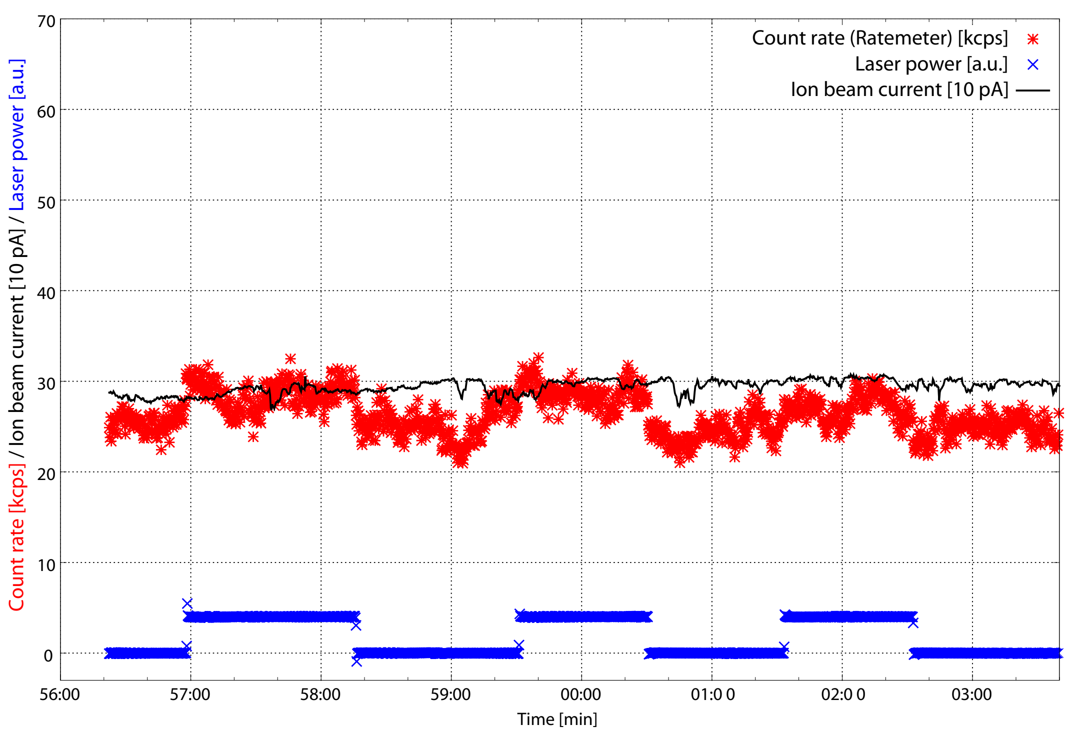

(b) Laser wavelength: $\lambda = 982\,\text{nm}$ ($\widehat{=}\, 1.263\,\text{eV}$). A slight difference of the output signal of the detector is observable when the laser is on and off, respectively.

Figure 5.1

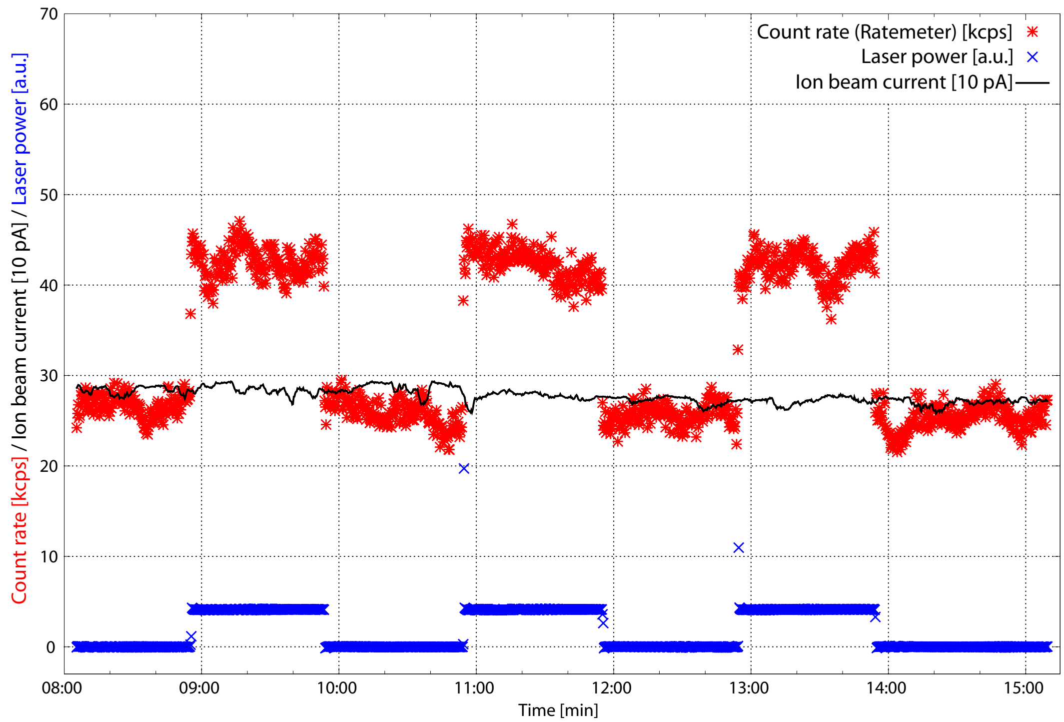

(c) Laser wavelength: $\lambda = 978\,\text{nm}$ ($\widehat{=} 1.269\,\text{eV}$). The count rate of the neutral particle detector clearly increases when the laser is on.

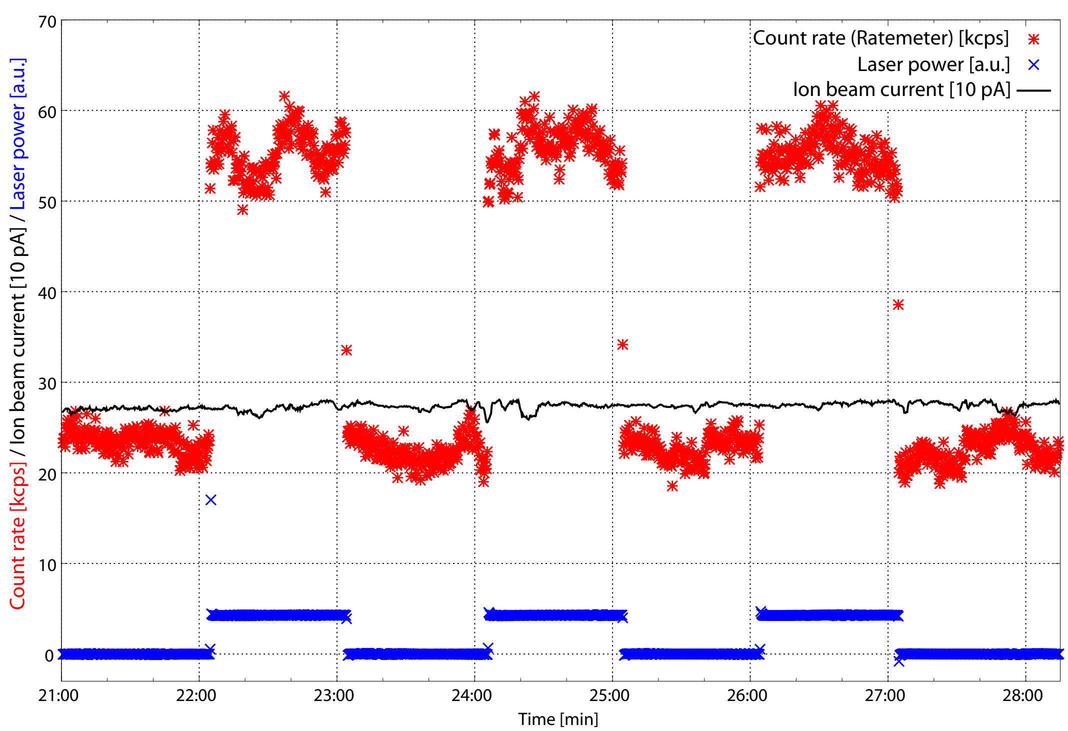

(d) Laser wavelength: $\lambda = 973\,\text{nm}$ ($\widehat{=} 1.275\,\text{eV}$). Further reduction of the laser wavelength yields again an increase of the count rate of the detector.

Figure 5.1: Photodetachment results for $^{12}C^{-}$. A successive reduction of the laser wavelength from $\lambda = 986\,\text{nm}$ ($\widehat{=} 1.258\,\text{eV}$) to $\lambda = 973\,\text{nm}$ ($\widehat{=} 1.275\,\text{eV}$) yields a clear increase of photodetached $^{12}C^{-}$ ions ($\text{EA}(^{12}C^{-}) = 1.262\,\text{eV}$).

5.2 $^{12}CH^-$

For the photodetachment studies with $^{12}CH^-$ again a 16 keV ion beam was tuned to FC 5. As mentioned in section 4.7, these molecular ions cause a significant higher background signal, hence, using slits prior the analyzing magnet, the beam current was reduced to approximately 50 pA in order not to overload the CEM. Furthermore, the device for precise overlap of the ion- and the laser beam was temporarily removed to investigate a possible influence on the background signal. Consequently, the background signal increased proportional to the ion beam current and, thus, no additional increase of the background signal caused by neutrals ejected from the specified device was observed. Hence, the photodetachment measurement was performed using the device for precise overlap of the ion- and the laser beam analog to the measurement of $^{12}C^-$. The laser wave length was set to $\lambda = 983$ nm ($\widehat{=}$ 1.262 eV), i.e. the laser energy was high enough to neutralize $^{12}CH^-$ (EA = 1.238 eV). The results of this measurement are shown in figure 5.2.

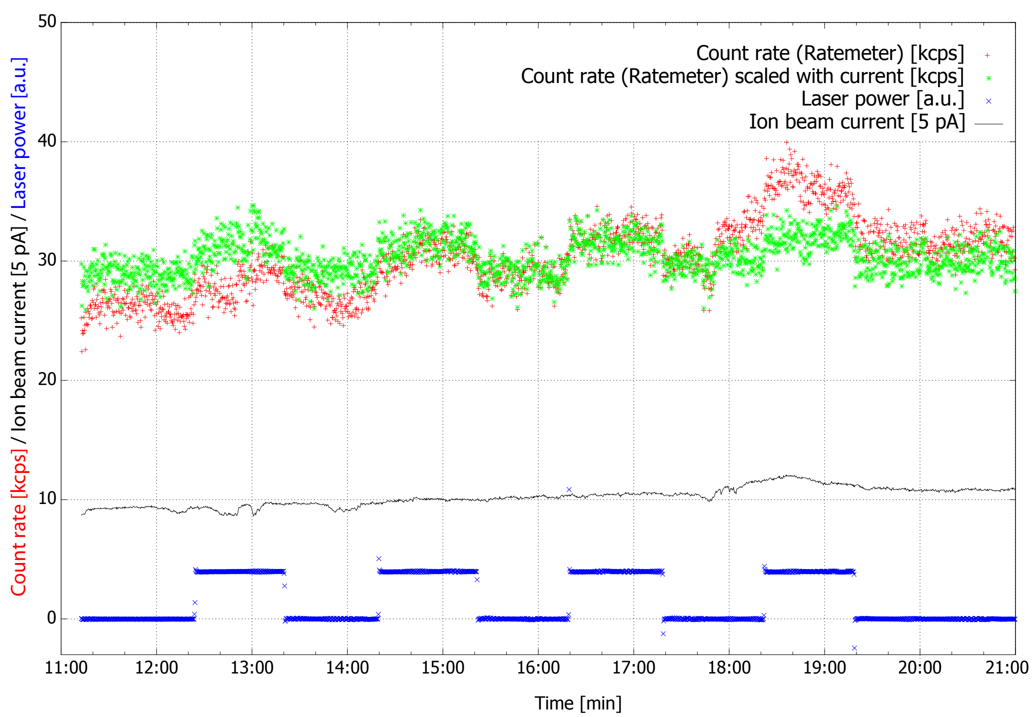

Figure 5.2: Photodetachment results for $^{12}CH^-$ (EA($^{12}CH^-$)=1.238 eV). The laser wavelength was set to $\lambda = 983$ nm ($\widehat{=}$ 1.262 eV). Molecular ion beams cause a much higher background signal than atomic ion beams, thus, the current has to be lowered in order not to overload the CEM. The measured count rates (red data points) were scaled with the fluctuating ion beam current to better show the photodetachment effect (green data points).

For as yet unknown reasons the current of the ion beam is slightly fluctuating affecting the measured count rates. In order to obtain a clear difference in the results when the laser is on and off, respectively, the measured count rates (plotted in red) were scaled with the ion beam current. Thus, despite the low ion beam current and the high background signal an explicit photodetachment effect is visible (Fig. 5.2).

5.3 $^{12}C^-$ versus $^{12}CH^-$

The results of the photodetachment measurements for $^{12}C^-$ and $^{12}CH^-$ presented in the previous sections are discussed in the following. The measured count rates of the neutral particle detector are converted to cps/pA in order to make them comparable for different ion beam currents.

It turned out that the count rate of the neutral particle detector increased up to 100 % for $^{12}C^-$ ions when the laser was on and the wavelength was set to $\lambda < 982$ nm (Fig. 5.1). This result corresponds to the estimations described in section 4.7 and 4.8. In the case of $^{12}CH^-$ the increase of the count rate in absolute numbers is similar but the background signal caused by collisional detachment of the electron is much higher (Tab. 5.1) as already discussed in section 4.7.

Laser \ Ion beam	$^{12}C^-$	$^{12}CH^-$
off	90 cps/pA	580 cps/pA
on	200 cps/pA	660 cps/pA
effect	110 cps/pA	80 cps/pA
Laser energy – EA	0.013 eV	0.024 eV

Table 5.1: Comparison of the results of $^{12}C^-$ and $^{12}CH^-$. The increase of the count rate in absolute numbers for $^{12}C^-$ and $^{12}CH^-$ ions is similar when the laser is on. However, the background signal caused by collisional detachment of the electron is much higher for $^{12}CH^-$.

5.4 Discussion and outlook

The goals of this thesis to design, construct, and test a neutral particle detector, to build an appropriate detection setup, and to neutralize atomic ($^{12}C^-$) and molecular ($^{12}CH^-$) anions, respectively, via laser photodetachment were successfully accomplished. Based on the results of the photodetachment studies of $^{12}C^-$ and $^{12}CH^-$ the following conclusions can be made:

- The setup described in chapter 4 works fine and fulfills the wanted requirements concerning ion beam tuning and detection. The installed detection setup (Fig. 4.1) was successfully tested and, thus, can be used as probe region for the measurement of the efficiency of selective suppression (Fig. 2.6) described in section 2.4. However, the reason for the fluctuations of the ion beam current measured with FC 5 (Fig. 4.1) and visible in the figures 5.1 and 5.2 has to be explored, as it is crucial for a stable operation of the rf quadrupole cooler.

- Simulations in SIMION 8.0 and the described measurements show that the time resolution of the developed neutral particle detector based on a conductively coated glass plate is <10 ns FWHM and that it is capable of measuring count rates up to some 10^6 cps, while the dark count rate is just in the order of some cps. Hence, the expected number of the neutralized particles during the measurement of the efficiency of selective suppression (section 2.4) is easily detectable.

- The reason for the different collisional detachment background signal for $^{12}C^-$ and $^{12}CH^-$ ions remains unclear. One explanation could be that neutralization by collisions with residual gas atoms is enhanced in the case of $^{12}CH^-$ due to excited molecular states. Further investigations are needed to explore whether this also applies for different molecular anions.
  In addition, the aperture to reduce the background signal caused by (secondary) electrons described in section 4.7 could be improved by adding a suppressor electrode. In the case that particles impinge on the edge of the drill hole the ejected electrons can currently be accelerated towards the neutral particle detector and cause an increase of the background signal.

- In order to achieve a high sensitivity for the measurement of the efficiency of selective suppression the background signal has to be lowered. It mainly depends on the pressure of the residual gas in the vacuum chamber and one can expect that a small fraction of the buffer gas of the radio frequency quadrupole ion cooler flows into the ultra high vacuum region of the beam line causing an increase of the pressure. Thus, the vacuum in the beam line has to be improved from 10^{-7}–10^{-8} to around 10^{-9} mbar.

The next steps in the ILIAS project will be the following:

- As the neutral particle detector is eventually positioned in the axis of the particle- and the laser beam, respectively, the setup has to be modified corresponding to figure 2.6 in order to test the detector under these conditions.

- The center piece of ILIAS, the radio frequency negative ion cooler, has to be implemented in the setup instead of the magnetic quadrupole doublet. Comprehensive tests and measurements will be required to maximize the transmission of the ion beam.

- As soon as the radio frequency negative ion cooler has been successfully tested a second laser will be installed to measure the efficiency of selective suppression (section 2.4).

Appendices

A | Engineering drawing of the used CEM

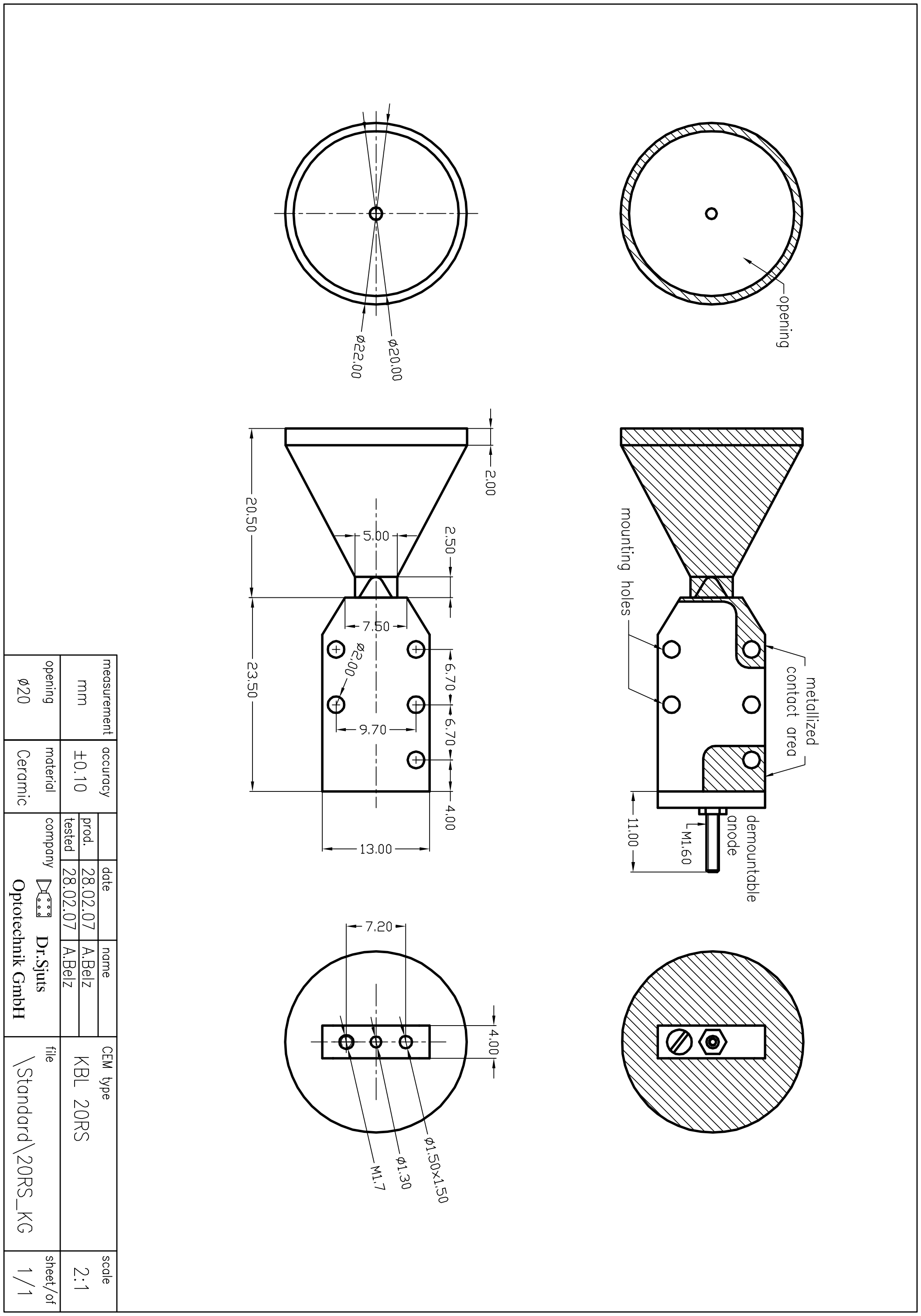

Figure A.1: Engineering drawing of the used CEM. Figure taken from [44].

B | Characteristics of standard CEMs

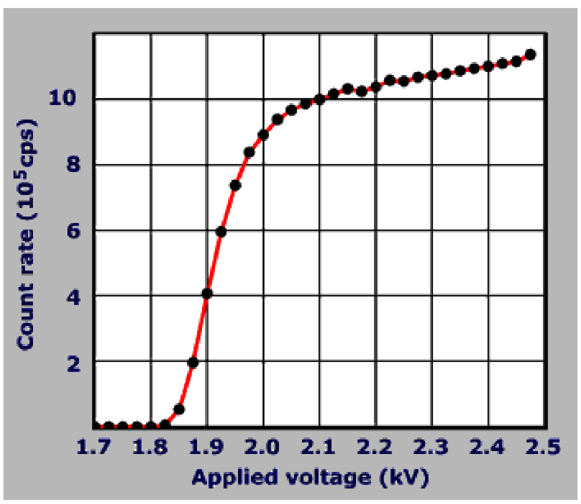

(a) Count rate vs. applied voltage.

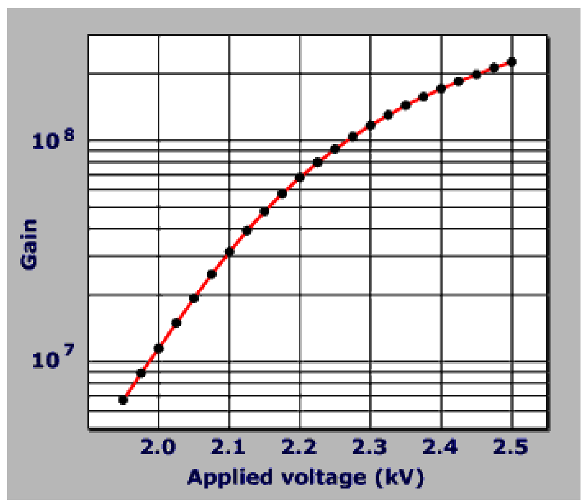

(b) Typical gain characteristic.

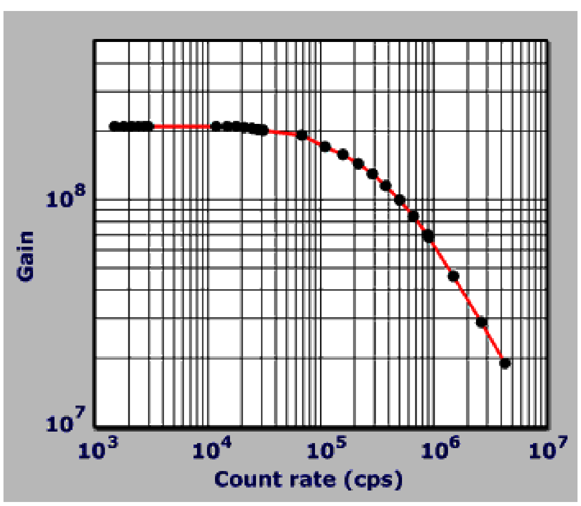

(c) Gain vs. count rate.

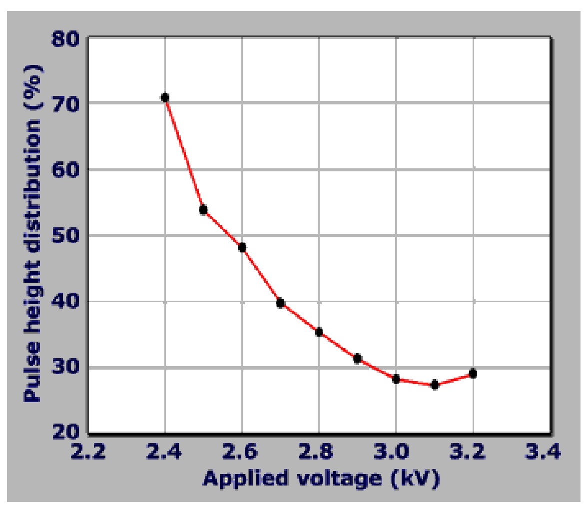

(d) Typical pulse height distribution vs. applied voltage

Figure B.1: Figures taken from [44].

C | Geometry file for SIMION

```
pa_define(101,51,61,p,n)

e(1)

;Glass plate
{

      fill  {     locate(10,5,1)     {
            within{ polyline(0,0,0,18,18,0)
                  }
            notin  { polyline(0,0,0,15,15,0)
                   }
                         }

            notin{ box3d(0,0,0,30,51,17.5)
                 }
            notin{ box3d(0,0,42.5,30,51,61)
                 }
           }


;Holder for glass plate

      fill  {     within { box3d(0,5,13,2,40,47)
                         }
            within{ box3d(2,5,13,30,40,15)
                  }
            within{ box3d(2,5,45,30,40,47)
                  }
            within{ box3d(28,32,15,30,40,45)
                  }
            }
}
```

```
e(2)

;Focus ring
{
      locate(45,25,30)    {

      rotate_fill(360)    {

             within{ polyline(0,0,5,0,5,12,0,12)
                   }
             notin  { polyline(0,0,5,0,5,10,0,10)
                   }

                          }
                          }
;Holder for focus ring

             locate(45,23,42)    {
             fill   {

             within { box3d(0,0,0,5,4,15)
                    }
             within { box3d(5,4,15,-45,0,20)
                    }
                   }

                                 }
}

e(3)

;Entrance of channel electron multiplier
{
      locate(55,25,30            {

      rotate_fill(360)    {
      within        {
                    polyline(0,0,0,13,22,0)
                    }

      notin         {
                    polyline(0,0,0,10,17,0)
                    }
                          }
                                 }
}

;e(4)

;Grounded cladding
;{
;     fill{  within{ box3d(0,0,0,101,51,1)
;                  }
;            within{ box3d(0,0,60,101,51,61)
;                  }
;            within{ box3d(0,0,0,101,1,61)
;                  }
;            within{ box3d(0,50,0,101,51,61)
;                  }
;
;          }
;}
```

D Engineering drawing of the quadrupole beam bender by DREEBIT

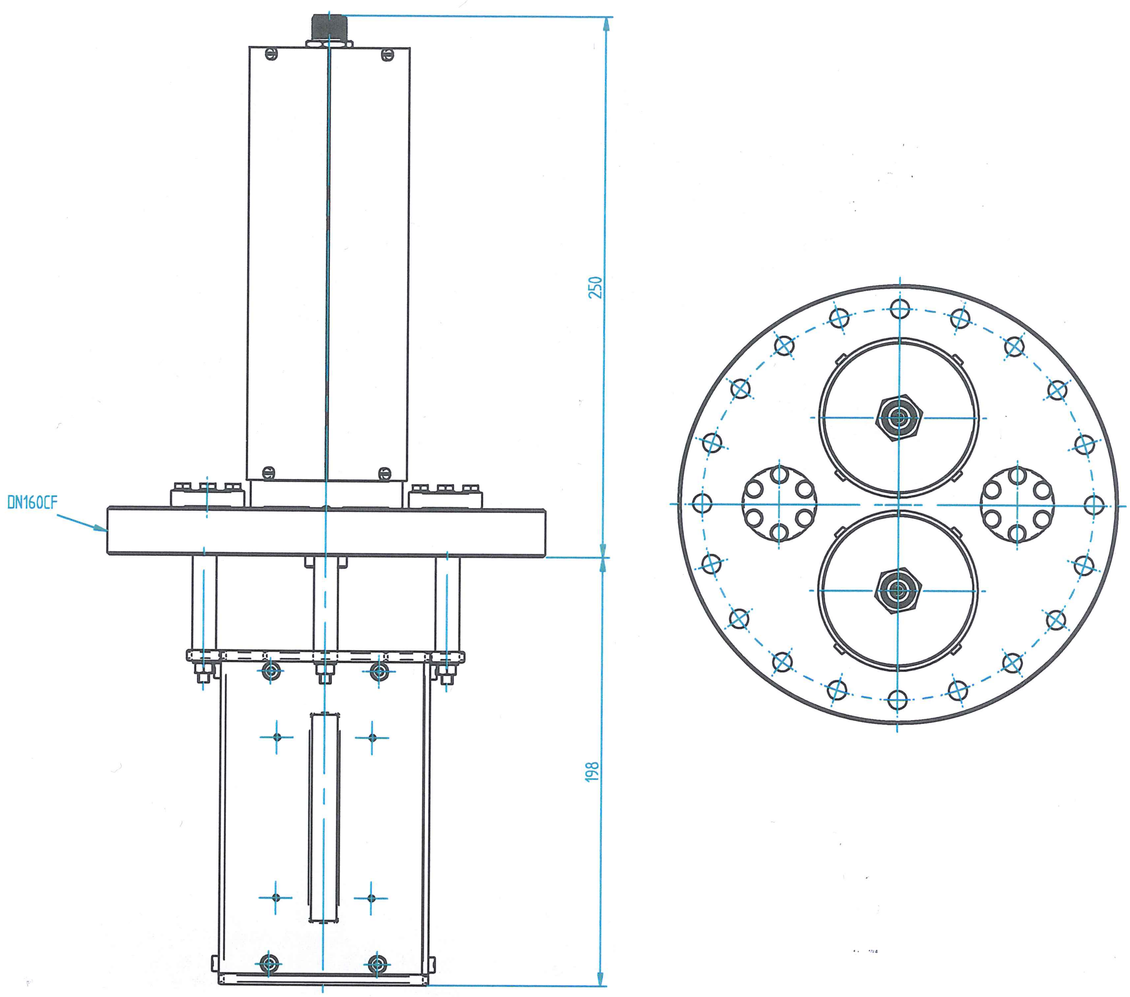

Figure D.1: Engineering drawing of the used quadrupole beam bender by DREEBIT. It has an overall height of 448 mm and is mounted on a standard CF160 flange. Figure taken from [47].

E Characteristics of the preamplifier WMT PAD01A

Case		
Aluminium (RF-shielded)	[mm]	89 x 35 x 30
Input signal (negative pulse)		
Amplitude into 50 Ω	[mV]	–3 to –1000
Safe operation without damage	[V]	±3
Pulse width (FWHM)	[ns]	5–20
Count rate (Poisson distribution)	[Hz]	up to $5{\cdot}10^5$
Resistance, dc-coupled	[Ω]	50
Threshold, screwdriver adjustable	[mV]	–3 to –100
Output signal (positive pulse)		
Resistance	[Ω]	50
Amplitude into high Z load	[V]	2.2
Amplitude into 50 Ω	[V]	1.1
Pulse width	[ns]	40 ± 10
Dead time	[ns]	80 ± 20
Power Supply		
Power supply (no signal, no load)	[V] [V]	+6 (±5 %), 24 mA typ. –6 (±5 %), 14 mA typ.
Temperature range		
For specified data	[°C]	10–40
For operation	[°C]	0–70

Table E.1: Characteristics of the used preamplifier PAD01A by WMT-Elektronik GmbH. Table taken from [44].

Bibliography

[1] Y. Liu, J.F. Liang, J.R. Beene, A high efficiency RF quadrupole ion beam cooler for negative ions, Nuclear Instruments and Methods in Physics Research B 255 (2007) 416–422.

[2] W. Kutschera , P. Collon, H. Friedmann, R. Golser, P. Hille, A. Priller, W. Rom, P. Steier, S. Tagesen, A. Wallner, E. Wild, G. Winkler, VERA: A new AMS facility in Vienna, Nuclear Instruments and Methods in Physics Research B 123 (1997) 47–50.

[3] W. Kutschera, Applications of accelerator mass spectrometry, International Journal of Mass Spectrometry 349-350 (2013) 203–218.

[4] O. Forstner, R. Golser, A. Priller, P. Steier, D. Hanstorp, H. Gnaser, Antrag für das Forschungsprojekt "Development of an ion beam cooler for selective optical filtering of negatively charged atomic and molecular ions".

[5] C. Dass, Fundamentals of Contemporary Mass Spectrometry, Wiley, 2007.

[6] L. K. Fifield, Accelerator mass spectrometry and its applications, Reports on Progress in Physics 62 (1999) 1223–1274.

[7] H. Synal, Developments in accelerator mass spectrometry, International Journal of Mass Spectrometry 349-350 (2013) 192–202.

[8] R. Hellborg, G. Skog, Accelerator mass spectrometry, Mass Spectrometry Reviews 27 (2008) 398–427.

[9] M. Martschini, P. Andersson, O. Forstner, R. Golser, D. Hanstorp, A.O. Lindahl, W. Kutschera, S. Pavetich, A. Priller, J. Rohlén, P. Steier, M. Suter, A. Wallner, AMS of ^{36}Cl with the VERA 3 MV tandem accelerator, Nuclear Instruments and Methods in Physics Research B 294 (2013) 115–120.

[10] J. Buchriegler, Construction of a Multi-Anode Ionization Chamber for AMS at VERA, Master's thesis, Universität Wien, 2013.

[11] K. Hain, Accelerator Mass Spectrometry Relevant for Nuclear Waste Transmutation, Master's thesis, Technische Universität München, 2011.

[12] D. Berkovits, E. Boaretto, G. Hollos, W. Kutschera, R. Naaman, M. Paul, Z. Vager, Selective suppression of negative ions by lasers, Nuclear Instruments and Methods in Physics Research A 281 (1989) 663–666.

[13] D. Berkovits, E. Boaretto, G. Hollos, W. Kutschera, R. Naaman, M. Paul, Z. Vager, Study of laser interaction with negative ions, Nuclear Instruments and Methods in Physics Research B 52 (1990) 378–383.

[14] O. Forstner, Progress of the ILIAS project for selective isobar suppression by laser photodetachment, DPG Conference 2012.

[15] Y. Liu, J.R. Beene, C.C. Havener, J.F. Liang, A.C. Havener, Isobar suppression by photodetachment in a gas-filled RF quadrupole ion guide, Applied Physics Letters 87 (2005) 113504.

[16] P. Andersson, A. O. Lindahl, D. Hanstorp, C. C. Havener, Yun Liu, Yuan Liu, Nearly complete isobar suppression by photodetachment, Journal of Applied Physics 107 (2010) 026102.

[17] J.C. Rienstra-Kiracofe, G.S. Tschumper, H.F. Schaefer, S. Nandi, G.B. Ellison, Atomic and Molecular Electron Affinities: Photoelectron Experiments and Theoretical Computations, Chemical Reviews 102 (2002) 231–282.

[18] A.E. Litherland, I. Tomski , X.-L. Zhao, Lisa M. Cousins, J.P. Doupé, G. Javahery, W.E. Kieser, Isobar separation at very low energy for AMS, Nuclear Instruments and Methods in Physics Research B 259 (2007) 230–235.

[19] J. Eliades, A.E. Litherland, W.E. Kieser, L. Cousins, S.J. Ye, X.-L. Zhao, Cl/S isobar separation using an on-line reaction cell for ^{36}Cl measurement at low energies, Nuclear Instruments and Methods in Physics Research B 268 (2010) 839–842.

[20] G. Rugel, T. Faestermann, K. Knie,G. Korschinek, M. Poutivtsev, D. Schumann, N. Kivel, I. Günther-Leopold, R. Weinreich, M. Wohlmuther, New Measurement of the ^{60}Fe Half-Life, Physical Review Letters 103 (2009) 072502.

[21] M. Limongi, A. Chieffi, Nucleosynthesis of ^{60}Fe in massive stars, New Astronomy Reviews 50 (2006) 474–476.

[22] J. Feige, A. Wallner, S.R. Winkler, S. Merchel, L.K. Filfield, G. Korschinek, G. Rugel, D. Breitschwerdt, The Search for Supernova-Produced Radionuclides in Terrestrial Deep-Sea Archives, Publications of the Astronomical Society of Australia 29, Issue 2 (2012) 109–114.

[23] K. Knie, S. Merchel, G. Korschinek, T. Faestermann, U. Herpers, M. Gloris, R. Michel, Accelerator mass spectrometry measurements and model calculations of iron-60 production rates in meteorites, Meteoritics & Planetary Science 34 (2009) 729–734.

[24] L. Fimiani, D.L. Cook, T. Faestermann, J.L. Gómez Guzmán, K. Hain, G.F. Herzog, G. Korschinek, B. Ligon, P. Ludwig, J. Park, R.C. Reedy, G. Rugel, Source of live ^{60}Fe, ^{10}Be, and ^{26}Al in Lunar Core 12025, Core 15008, Skim Sample 69921, Scoop Sample 69941, and under-boulder Sample 69961, 43rd Lunar and Planetary Science Conference, held at The Woodlands, Texas. LPI Contribution No. 1659, id.1279, March 19-23, 2012.

[25] K. Knie, G. Korschinek, T. Faestermann, E. A. Dorfi, G. Rugel, A.Wallner, ^{60}Fe Anomaly in a Deep-Sea Manganese Crust and Implications for a Nearby Supernova Source, Physical Review Letters 93 (2004) 171103.

[26] P. Gartenmann, C. Schnabel, M. Suter, H.-A. Synal, ^{60}Fe measurements with an EN tandem accelerator, Nuclear Instruments and Methods in Physics Research B 123 (1997) 132–136.

[27] C. Vockenhuber, F. Oberli, M. Bichler, I. Ahmad, G. Quitté, M. Meier, A.N. Halliday, D.-C. Lee, W. Kutschera, P. Steier, R.J. Gehrke, R.G. Helmer, New Half-Life Measurement of ^{182}Hf: Improved Chronometer for the Early Solar System, Physical Review Letters 93 (2004) 172501.

[28] C. Vockenhuber, M. Bichler, R. Golser, W. Kutschera, A. Priller, P. Steier, S. Winkler, ^{182}Hf, a new isotope for AMS, Nuclear Instruments and Methods in Physics Research B 223-224 (2004) 823–828.

[29] O. Forstner, H. Gnaser, D. Hanstorp, M. Martschini, A. Priller, J. Rohlén, P. Steier, C. Vockenhuber, A. Wallner, Reassessment of ^{182}Hf AMS measurements at VERA, Nuclear Instruments and Methods in Physics Research B 269 (2011) 3180–3182.

[30] P. Andersson, O. Forstner, D. Hanstorp, A.O. Lindahl, K. Wendt, Isobar Selectiv Laser Photodetachment In Trace Element Analysis, AIP Conference Proceedings 1104 (2009) 53–60.

[31] T. Leopold, J. Rohlén, P. Andersson, C. Diehl, M. Eklund, O. Forstner, D. Hanstorp, H. Hultgren, P. Klason, A.O. Lindahl, K. Wendt, Feasibility of photodetachment isobar suppression of WF_5^- with respect to HfF_5^-, International Journal of Mass Spectrometry 359 (2014) 12–18.

[32] National Electrostatics Corporation, `http://www.pelletron.com/negion.htm`.

[33] S. Pavetich, AMS measurement of the reaction ^{35}Cl(n,γ)^{36}Cl and its relevance to astrophysics and nuclear technology, Master's thesis, Universität Wien, 2011.

[34] Y. Liu, J.F. Liang, G.D. Alton, J.R. Beene, Z. Zhou, H. Wollnik, Collisional cooling of negative-ion beams, Nuclear Instruments and Methods in Physics Research B 187 (2002) 117–131.

[35] ORTEC Products Group, `http://www.ortec-online.com/`.

[36] S. Gotoh, Z. Takagi, Silicon Surface Barrier Detector, Nuclear Science and Technology 1, No. 8 (1964) 311–315.

[37] G. F. Knoll, Radiation detection and measurement, Wiley, 1989.

[38] S. Lausberg, Development of a Metallic Magnetic Calorimeter for High Resolution β-Spectroscopy, Master's thesis, Ruprecht-Karls-Universität Heidelberg, 2008.

[39] SPIE international society for optics and photonics, `http://spie.org/x39001.xml`.

[40] O. Novotny, S. Allgeier, L. Gamer, D. Hengstler, S. Kempf, C. Krantz, A. Pabinger, C. Pies, D. W. Savin, D. Schwalm, C. Enss, A. Fleischmann, A. Wolf, Cryogenic microcalorimeter energy resolution measurements for multi-keV atoms and molecules., DPG Conference 2014.

[41] W. E. Baumgartner, W. K. Huber, Secondary electron emission multipliers as particle detectors, Journal of Physics E: Scientific Instruments 9 (1976) 321–330.

[42] Sigma-Aldrich Foundation, http://www.sigmaaldrich.com/catalog/product/aldrich/703176?lang=de&region=AT.

[43] C. Vockenhuber, Entwicklung eines Foliendetektors zur Teilchenidentifizierung für AMS, Master's thesis, Universität Wien, 1999.

[44] Dr. Sjuts Optotechnik GmbH, www.sjuts.com.

[45] Dassault Systèmes SolidWorks Corp., www.solidworks.com.

[46] DREEBIT GmbH, www.dreebit.com.

[47] Dreebit, Instruction Manual Quadrupole Beam Bender, Version: 1.0, 13.03.2013.

[48] Changchun New Industries Optoelectronics Technology Co., Ltd., www.cnilaser.com.

[49] R.F. Nascimento, S.L.A. Mello, B.F. Magnani, M.M. Sant´ Anna, G. Jalbert, N.V. de Castro Faria, Total detachment cross sections of C^-, CH^-, C_2^- , and C_2H^- incident on N_2 at keV energies, Physical Review A 87 (2013) 062704.

[50] G. Haeffler, D. Hanstorp, I. Yu Kiyan, U. Ljungblad, H.H. Andersen, T. Andersen, Photodetachment cross sections for the ^4S bound state of the negative carbon ion, Journal of Physics B: Atomic, Molecular and Optical Physics 29 (1996) 3017–3022.

Acknowledgments

First I want to thank Prof. Robin Golser for suggesting the topic of this Master's thesis, for realizing my assets and limitations, and for the consequential informative and constructive feedback, review, and response concerning various tasks during this period. Also, I want to thank him for helpful advices on my job search.

Furthermore, I want to thank:

Martin Martschini for the support during the installation of the detection setup, for helping me with the measurement performance and the evaluation of the results. Besides, I want to thank him for his patience in answering all my questions concerning nuclear physics and especially for proofreading and constructive feedback.

Alfred Priller for helping me with the construction of the detector and other components with Solid Works and SIMION, for proofreading, and for interesting discussions and explanations using creative metaphors.

Oliver Forstner for instructing me in the basic principles of ILIAS, for sharing his experience in ion beam tuning, and for supporting me with the setup of the detector.

Peter Steier for helping me to put the glove box into operation.

Jenny Feige for countless Latex advices and for helping me with Mathematica. Also, I want to thank her for interesting discussions during breaks, for proofreading my job application, and for frequently provided fresh fruits.

Johanna Pitters for sharing her knowledge of VERA and nuclear physics and for proofreading my job application.

Johannes Lachner for IT support and for sharing his knowledge about nuclear physics and his recipe for Obazda.

The staff in the VERA workshop, Ewald Friedl, Johann Lukas, Wolfgang Hieß, and Gabriela Obstmayer for professional manufacturing of various components and helpful suggestions for improvement concerning efficient setup.

My family and especially my parents who always supported me in every sense and enabled me to have an interesting and diversified life during university studies.

Julia Mayerhofer, my life companion, who always motivated and inspired me, especially by demonstrating how to compose a Master's thesis very efficiently. Furthermore, she was always understanding and supported me through difficult times during my studies. Thank you very much! You are my favorite proton!

Curriculum vitae

Name:	**Johannes Lahner**
Place of birth:	Mistelbach
Nationality:	Austria

Education

since 01/2013:	Master's thesis at the Faculty of Physics (Isotope Research and Nuclear Physics) at the University of Vienna, supervisor: Prof. Robin Golser: *A neutral particle detector for photodetachment studies*
since 10/2012:	Master's degree in physics
2005 – 2012:	Bachelor's degree in physics
1997 – 2003:	Federal Secondary College of Electrical Engineering (HTBLA Wien Donaustadt), Graduation 06/2003
1993 – 1997	Secondary school in Wolkersdorf
1989 – 1993	Elementary school in Kreuzstetten

Work experience

11/2012 – 02/2014	Tutor for physics and mathematics
08/2005	Claq Watertech: Manual manufacturing of bioactive filters for swimming pools
09/2004 – 11/2004	Mastermanagement: Customer service for the publishing group News
07/2000, 07/2002	GHG Elektronik: Installation and service of CO-warning devices
07/1998	Ligna-Team Montagen G.m.b.H.: Installation of windows and doors